NATIONAL AERONAUTICS AND SPACE ADMINISTRATION

Technical Memorandum 33-753

On the Thermoelastic Analysis of Solar Cell Arrays and Related Material Properties

M. A. Salama

F. L. Bouquet

JET PROPULSION LABORATORY

CALIFORNIA INSTITUTE OF TECHNOLOGY

PASADENA, CALIFORNIA

February 15, 1976

1. Report No. 33-753	2. Government Accession No.	3. Recipient's Catalog No.

4. Title and Subtitle ON THE THERMOELASTIC ANALYSIS OF SOLAR CELL ARRAYS AND RELATED MATERIAL PROPERTIES	5. Report Date February 15, 1976
	6. Performing Organization Code

7. Author(s) M. A. Salama, F. L. Bouquet	8. Performing Organization Report No.

9. Performing Organization Name and Address JET PROPULSION LABORATORY California Institute of Technology 4800 Oak Grove Drive Pasadena, California 91103	10. Work Unit No.
	11. Contract or Grant No. NAS 7-100
	13. Type of Report and Period Covered Technical Memorandum

12. Sponsoring Agency Name and Address NATIONAL AERONAUTICS AND SPACE ADMINISTRATION Washington, D.C. 20546	
	14. Sponsoring Agency Code

15. Supplementary Notes

16. Abstract

Accurate prediction of failures of solar cell arrays requires corresponding accuracy in the computation of their thermally induced stresses. This was accomplished by using the finite element technique. Certain improvements in the previously reported procedures for stress calculation were introduced together with failure criteria capable of describing a wide range of ductile and brittle material behavior. With these improvements and capabilities, the stress distribution and associated failure mechanisms in the N-interconnect junction of two JPL solar cell designs were discussed and correlated to previous findings.

In such stress and failure analysis, it is essential to know the thermomechanical properties of the materials involved. To complement previous efforts in this direction, new measurements were made of properties of materials suitable for the design of lightweight arrays: namely, the microsheet-0211 glass material for the solar cell filter together with five materials for lightweight substrates (Kapton-H, Kapton F, Teflon, Tedlar, and Mica Ply PG-402). The temperature-dependence of the thermal coefficient of expansion for these materials was determined together with other key properties such as the elastic moduli, Poisson's ratio, and the stress-strain behavior up to failure.

17. Key Words (Selected by Author(s)) Nonmetallic Materials Structural Mechanics Energy Production and Conversion Numerical Analysis	18. Distribution Statement Unclassified -- Unlimited

19. Security Classif. (of this report) Unclassified	20. Security Classif. (of this page) Unclassified	21. No. of Pages 78	22. Price

HOW TO FILL OUT THE TECHNICAL REPORT STANDARD TITLE PAGE

Make items 1, 4, 5, 9, 12, and 13 agree with the corresponding information on the report cover. Use all capital letters for title (item 4). Leave items 2, 6, and 14 blank. Complete the remaining items as follows:

3. Recipient's Catalog No. Reserved for use by report recipients.

7. Author(s). Include corresponding information from the report cover. In addition, list the affiliation of an author if it differs from that of the performing organization.

8. Performing Organization Report No. Insert if performing organization wishes to assign this number.

10. Work Unit No. Use the agency-wide code (for example, 923-50-10-06-72), which uniquely identifies the work unit under which the work was authorized. Non-NASA performing organizations will leave this blank.

11. Insert the number of the contract or grant under which the report was prepared.

15. Supplementary Notes. Enter information not included elsewhere but useful, such as: Prepared in cooperation with... Translation of (or by)... Presented at conference of... To be published in...

16. Abstract. Include a brief (not to exceed 200 words) factual summary of the most significant information contained in the report. If possible, the abstract of a classified report should be unclassified. If the report contains a significant bibliography or literature survey, mention it here.

17. Key Words. Insert terms or short phrases selected by the author that identify the principal subjects covered in the report, and that are sufficiently specific and precise to be used for cataloging.

18. Distribution Statement. Enter one of the authorized statements used to denote releasability to the public or a limitation on dissemination for reasons other than security of defense information. Authorized statements are "Unclassified—Unlimited, " "U. S. Government and Contractors only, " "U. S. Government Agencies only, " and "NASA and NASA Contractors only. "

19. Security Classification (of report). NOTE: Reports carrying a security classification will require additional markings giving security and down-grading information as specified by the Security Requirements Checklist and the DoD Industrial Security Manual (DoD 5220.22-M).

20. Security Classification (of this page). NOTE: Because this page may be used in preparing announcements, bibliographies, and data banks, it should be unclassified if possible. If a classification is required, indicate separately the classification of the title and the abstract by following these items with either "(U)" for unclassified, or "(C)" or "(S)" as applicable for classified items.

21. No. of Pages. Insert the number of pages.

22. Price. Insert the price set by the Clearinghouse for Federal Scientific and Technical Information or the Government Printing Office, if known.

TECHNICAL REPORT STANDARD TITLE PAGE

1. Report No. 33-753	2. Government Accession No.	3. Recipient's Catalog No.

4. Title and Subtitle	5. Report Date
	6. Performing Organization Code

7. Author(s)	8. Performing Organization Report No.

9. Performing Organization Name and Address	10. Work Unit No.
JET PROPULSION LABORATORY California Institute of Technology 4800 Oak Grove Drive Pasadena, California 91103	11. Contract or Grant No. NAS 7-100
	13. Type of Report and Period Covered

12. Sponsoring Agency Name and Address	
NATIONAL AERONAUTICS AND SPACE ADMINISTRATION Washington, D.C. 20546	14. Sponsoring Agency Code

15. Supplementary Notes

16. Abstract

With the failure analysis and supporting material property characterization, this work presents a significant advance in the capability of designing solar cell arrays.

17. Key Words (Selected by Author(s))	18. Distribution Statement

19. Security Classif. (of this report)	20. Security Classif. (of this page)	21. No. of Pages	22. Price

HOW TO FILL OUT THE TECHNICAL REPORT STANDARD TITLE PAGE

Make items 1, 4, 5, 9, 12, and 13 agree with the corresponding information on the report cover. Use all capital letters for title (item 4). Leave items 2, 6, and 14 blank. Complete the remaining items as follows:

3. Recipient's Catalog No. Reserved for use by report recipients.

7. Author(s). Include corresponding information from the report cover. In addition, list the affiliation of an author if it differs from that of the performing organization.

8. Performing Organization Report No. Insert if performing organization wishes to assign this number.

10. Work Unit No. Use the agency-wide code (for example, 923-50-10-06-72), which uniquely identifies the work unit under which the work was authorized. Non-NASA performing organizations will leave this blank.

11. Insert the number of the contract or grant under which the report was prepared.

15. Supplementary Notes. Enter information not included elsewhere but useful, such as: Prepared in cooperation with... Translation of (or by)... Presented at conference of... To be published in...

16. Abstract. Include a brief (not to exceed 200 words) factual summary of the most significant information contained in the report. If possible, the abstract of a classified report should be unclassified. If the report contains a significant bibliography or literature survey, mention it here.

17. Key Words. Insert terms or short phrases selected by the author that identify the principal subjects covered in the report, and that are sufficiently specific and precise to be used for cataloging.

18. Distribution Statement. Enter one of the authorized statements used to denote releasability to the public or a limitation on dissemination for reasons other than security of defense information. Authorized statements are "Unclassified—Unlimited, " "U. S. Government and Contractors only, " "U. S. Government Agencies only, " and "NASA and NASA Contractors only. "

19. Security Classification (of report). NOTE: Reports carrying a security classification will require additional markings giving security and down-grading information as specified by the Security Requirements Checklist and the DoD Industrial Security Manual (DoD 5220.22-M).

20. Security Classification (of this page). NOTE: Because this page may be used in preparing announcements, bibliographies, and data banks, it should be unclassified if possible. If a classification is required, indicate separately the classification of the title and the abstract by following these items with either "(U)" for unclassified, or "(C)" or "(S)" as applicable for classified items.

21. No. of Pages. Insert the number of pages.

22. Price. Insert the price set by the Clearinghouse for Federal Scientific and Technical Information or the Government Printing Office, if known.

PREFACE

The work described in this report was performed by the Applied Mechanics and the Guidance and Control Divisions of the Jet Propulsion Laboratory.

ACKNOWLEDGMENT

CONTENTS

TABLES

FIGURES

ABSTRACT

Accurate prediction of failures of solar cell arrays requires corresponding accuracy in the computation of their thermally induced stresses. This was accomplished by using the finite element technique. Certain improvements in the previously reported procedures for stress calculation were introduced together with failure criteria capable of describing a wide range of ductile and brittle material behavior. With these improvements and capabilities, the stress distribution and associated failure mechanisms in the N-interconnect junction of two JPL solar cell designs were discussed and correlated to previous findings.

In such stress and failure analysis, it is essential to know the thermomechanical properties of the materials involved. To complement previous efforts in this direction, new measurements were made of properties of materials suitable for the design of lightweight arrays: namely, the microsheet-0211 glass material for the solar cell filter together with five materials for lightweight substrates (Kapton-H, Kapton F, Teflon, Tedlar, and Mica Ply PG-402). The temperature-dependence of the thermal coefficient of expansion for these materials was determined together with other key properties such as the elastic moduli, Poisson's ratio, and the stress-strain behavior up to failure.

With the failure analysis and supporting material property characterization, this work presents a significant advance in the capability of designing solar cell arrays.

I. INTRODUCTION

During their lifetimes, solar cells can be subjected to a variety of environmental conditions, the most hostile of which involves large thermal excursions of a cyclic nature. Large thermal variations are particularly damaging to the integrity of solar cells. A most familiar factor contributing to this is the fact that a solar cell typically consists of several components, such as the filter glass cover, interconnects, solder, silicon wafer, coatings, adhesives, and substrate. Each of these is made of a different material, with thermomechanical properties different from the others, giving rise to high stresses and subsequent mechanical failures when large thermal excursions are involved.

A less familiar but potentially very important factor that can contribute to sudden high stresses and subsequent failure is the rate of change of certain key properties, such as the material elasticity modulus and coefficient of thermal expansion, as temperature is changed. Adhesives used for bonding the filter glass cover to the silicon solar cell and the silicon solar cell itself to the supporting substrate tend to go through several phase transitions at certain temperatures, as do polymeric materials used as substrates for lightweight solar arrays. Depending on the material and temperature, there could be mild or drastic property changes associated with these transitions. The greater the range of temperature excursion, the greater the chance of encountering one or more of these phase transitions. Considering what could take place simultaneously in the neighboring materials, the net result may be either a stress relief or a stress concentration, leading to possible mechanical failure.

In view of these important possibilities, and because of current emphasis on producing highly reliable solar cell designs, characterizing the temperature-dependence of the solar cell material properties and predicting their stresses and associated failures as accurately as possible are of central importance. This requires an accurate determination of material behavior throughout the temperature range of interest as well as an accurate computational scheme that can account for property changes of both short and long durations.

Previous efforts in this direction are described in Refs. 1 and 2, which represent successive levels of improvements. The first part of this report draws heavily upon the basic finite element method of analysis used in Ref. 2, with special emphasis on several improvements in the accuracy of stress computation and criteria for failure prediction in various materials. The second part includes a comprehensive description of the thermomechanical properties of the microsheet-0211 glass material used for solar cell filter, along with five materials used as substrates for lightweight solar cell arrays. The material property characterizations elucidated in Ref. 2[1] and extended herein serve

---

[1]Included in Ref. 2 are descriptions of the thermomechanical properties of the P- and N-type silicon material for the solar cells and various materials for the interconnect metals. A solder alloy and several candidate silicone rubber adhesives are also included.

as a relatively complete data base for the more accurate stress computation and failure prediction procedure detailed next. The procedure is then applied to the thermal stresses in the N-interconnect junction in two JPL solar cell designs.

II. THERMOELASTIC STRESS ANALYSIS

A. BACKGROUND

Accurate prediction of solar cell failures requires accurate computation of thermally induced stresses. In previous work (Refs. 1 and 2), successive levels of improvements in the stress computation and in the required material property data were presented. The need for these improvements resulted from the following considerations:

(1)   The variety of materials and design configurations involved in a typical solar cell array makes it difficult to perform an accurate failure analysis of the array components by simplified closed form analytical means. Thus, the finite element analysis approach was used (Ref. 1), with the usual assumptions of elastic material behavior. The "ELAS" computer program was employed as the computational tool.

(2)   In a conventional elastic regime, thermal stresses are obtained in a single solution step during which the material properties are assumed independent of the thermal disturbances. While this assumption is valid and can yield accurate results when used with small thermal variations or with materials that exhibit slight changes in properties with temperature changes, it becomes invalid and leads to large errors as the actual behavior deviates from these assumptions. In a space environment, thermal excursion greater than 200°C can be expected during a typical thermal cycle. In addition, while the properties of some materials such as silicon and fused silica are not strongly dependent upon temperature, the properties of others such as solder, silver, Kovar, and silicones are extremely sensitive to thermal changes. Materials with both characteristics are used together as integrated components of a typical solar cell array.

In view of these considerations, the conventional elastic analysis of Ref. 1 was extended to the thermoelastic analysis in Ref. 2. In the latter, emphasis was placed on the determination of complete sets of thermomechanical properties for materials of the solar cell array components, along with the use of the VISCEL computer program for the thermoelastic stress analysis. In VISCEL, components of a given solar cell configuration are modeled as a system of finite elements connected together at nodal points. A typical cycle is then simulated by a series of successive temperature increments or decrements, during which the material properties are allowed to change from one increment to the next. The corresponding deformations and stresses are computed for each increment on a cumulative basis. In this computational scheme, the thermomechanical material properties such as those discussed in Section IV are used as input data for each temperature increment.

B. IMPROVEMENTS IN THE STRESS ANALYSIS

The thermoelastic stress and failure analysis described above has been successfully applied to various solar cell configurations (Ref. 2). However, a close examination of the reported thermomechanical properties of components of the solar cell materials together with results of the stress and failure analysis suggests certain improvements.

1. Intermaterial Boundary Stresses

In the composite makeup of a solar cell, flexible materials like the silicones at room temperature or higher, or solder at above room temperature, are integrated with stiffer materials like fused silica, silicon, and most metals for the interconnectors. Depending on the operating temperature, orders of magnitude difference may be observed (Ref. 2) between properties such as the elastic modulus E for the stiff vs the flexible materials. For example, at $0°C$, E (7940 silica) $= 7 \times 10^6$ N/cm^2 and E(RTV-560 silicone) $= 3 \times 10^2$ N/cm^2. Such drastic differences in the stiffness-related properties give rise to errors in the stresses computed at the intermaterial boundary points when the conventional procedures of finite element stress calculations are used.

In a conventional finite element procedure, stresses are computed from the conditions of deformation compatibility and constitutive stress-strain relationships. In conjunction with these necessary conditions, various schemes of stress averaging, best fit strains, and virtual strains have been recommended. Stresses obtained by these procedures do not necessarily satisfy the conditions of force equilibrium, especially at the intermaterial boundary points. Stronger violation of the conditions of force equilibrium is associated with greater difference between the properties of adjacent materials as was cited above.

The approach taken here utilizes a generalization of the method of best fit strain tensor for the stress computation at intermaterial boundary points, so that deformation compatibility and constitutive relationships as well as equilibrium conditions are satisfied. The approach was developed for the present work. A detailed description of its theoretical basis is given in Appendix A.

2. Failure Criteria

Once the stresses have been computed throughout a given solar cell model, it is important to assess the possibility of its mechanical failure due to these stresses. Such failures can occur either by ductile inelastic deformation and subsequent loss of useful strength or by brittle fracture. The first mode of failure is characteristic of most metals for the solar cell interconnector as well as the solder and the silicone adhesives. However, for silicone adhesives and most polymers at temperatures below their glass transition temperature, as well as for all ceramics such as fused silica, microsheet 0211 and silicon, failure by brittle fracture is most likely. These conclusions become evident upon examination of the stress-strain curves reported in Section IV-B-4 as well as those of Ref. 2. It also becomes evident that while ductile inelastic failure may be the prominent mode in a compressive stress state, brittle fracture may be expected of the same material under the same temperature

when the same stresses are reversed from compressive to tensile. In Ref.
2, Figs. 25 and 28 for RTV-silicones at -184 and -25°C are examples. An
additional complication arises from the fact that the tensile strength of
brittle materials like ceramics and silicones below their glass transition
temperature is about 8 to 5 times smaller than their compressive strength
(see Tables 2 and 3 of Ref. 2).

The above complications made it desirable to have several options of
failure criteria available to the designer in the VISCEL computer program.
These options are provided by computing the stress parameters described in
(1), (2), and (3) below.

Given a material point, let σ_x, σ_y, σ_z, T_{xy}, T_{xz}, and T_{yz} be the three
normal and three shear stresses. Then,

(1)   Upon computing the principal stresses σ_1, σ_2, and σ_3,
        where $\sigma_1 > \sigma_2 > \sigma_3$, the maximum normal stress criterion can be applied
        by comparing σ_1 with the ultimate strength $\sigma*$ of the material.
        This criterion is suitable for predicting failure by brittle
        fracture.

(2)   The maximum shear stress criterion is provided as an alternative
        criterion for the prediction of failure in ductile materials for
        the interconnectors. This is given by comparing the maximum shear
        stress values $(\sigma_1 - \sigma_3)$ to the yield stress $\sigma*$. The ratio
        $R_1 = (\sigma_1 - \sigma_3)/\sigma*$ is printed out by the computer program upon
        request.

(3)   The most suitable criterion among the various options is provided
        by introducing a generalized form of the Von Mises failure criterion
        (Ref. 3), which is capable of describing the failure of materials
        having different strengths in compression from those in tension.
        It states that if

        S_T = yield stress in a uniaxial tensile test

        where

            $\sigma_x = S_T$, and $\sigma_y = \sigma_z = T_{xy} = T_{yz} = T_{zx} = 0$

        and

        S_C = same as S_T except that it is the compressive value

        and

            $k = -(S_C/S_T)$ = ratio of compressive to tensile strength

        then according to this theory, the material point will fail when

$$1/2[(\sigma_x - \sigma_y)^2 + (\sigma_y - \sigma_z)^2 + (\sigma_z - \sigma_x)^2 + 6(T_{xy}^2 + T_{yz}^2 + T_{zx}^2)]$$
$$+ (k-1)(\sigma_x + \sigma_y + \sigma_z) S_T - kS_T^2 = 0 \qquad (1)$$

When k = 1, the above expression reduces to the usual Von Mises criterion; otherwise the expression represents a paraboloid of revolution with its axes along the line $\sigma_x = \sigma_y = \sigma_z$. Therefore, it represents a Griffith-type criterion. The fact that the theory admits values of k > 1 implies its ability to describe the failure of brittle materials. The tensile strengths of these materials (silicon as an example) are typically smaller than their compressive strengths because they typically contain microcracks, pores and flaws. Under tensile loads these defects open up and propagate to failure faster than under compressive loads. This criterion is implemented in VISCEL by the following procedure:

(1)   After the stresses σ_x, σ_y, σ_z, T_{xy}, T_{yz}, and T_{zx} have been computed at a material point whose S_T and k are known, the largest of these six stress components is identified and its absolute value is called σ.

(2)   Form the nondimensional stress quantities $\sigma_x/\sigma = \alpha_{11}$, $\sigma_y/\sigma = \alpha_{22}$,

$\sigma_z/\sigma = \alpha_{33}$, $T_{xy}/\sigma = \alpha_{12}$, $T_{yz}/\sigma = \alpha_{23}$, and $T_{zx}/\sigma = \alpha_{31}$ with their

respective algebraic sign retained.

(3)   The resulting expression for the failure criteria is

$$(\sigma^2/2) \ [(\alpha_{11} - \alpha_{22})^2 + (\alpha_{22} - \alpha_{33})^2 + (\alpha_{33} - \alpha_{11})^2 + 6(\alpha_{12}{}^2 +$$

$$\alpha_{23}{}^2 + \alpha_{31}{}^2)] + \sigma(k-1) \ (\alpha_{11} + \alpha_{22} + \alpha_{33}) \ S_T - kS_T{}^2 = 0 \qquad (2)$$

whose positive root for a given S_T and k is computed and is called σ^*. The ratio $R2 = |\sigma/\sigma^*|$ is then calculated and printed out.

Then failure takes place when $R_2 \geq 1.0$.

C.   DATA PREPARATION FOR VISCEL COMPUTER PROGRAM

The improvements described in the previous section and Appendix A were implemented in the VISCEL computer program on JPL's Univac 1108 system. A thorough description of the original form of the program (without the improvements) has been documented in Refs. 4 and 5. In this section, only the improvements and those portions of the program that were affected by them will be discussed.

As mentioned previously, the important difference between the improved and the original version of VISCEL is in the manner of stress computation at the intermaterial boundary and in the availability of additional failure criteria. So far, these have been implemented for finite elements suitable for plane-stress, plane-strain, and general solids. For solar cells these are the most useful elements. The new version of the program has additional segments for stress computation called LINK4A, which consists of 21 subroutines. This new segment is activated when certain parameters are encountered at the end of the usual input data required for the original version of the program (Ref. 5).

A first stage in the data preparation for the new version of the program involves the preparation of exactly the same set of inputs required for the

original VISCEL, according to Refs. 4 and 5. These include such items as problem control parameters, an initial set of material properties, pressures and forces, temperatures and their gradients, geometry descriptions such as nodal coordinates, element connections, and boundary conditions, and finally a literal 1END (card columns 77-80), declaring the end of information necessary for the initial zero step of the solution. Subsequent first, second..., and i solution steps involve adding the new set of modifiable data for each of the first, second...., and i solution steps. Each of these is followed by its literal 1END card. Only the last solution step ends with END, without a prefix integer. If the user desires to obtain the same output of the original VISCEL program without any of the improvements described previously, he would not need to supply any further input data.

To activate the new stress link, the second stage of data preparation requires the modification of all of the 1END cards, according to the following rules. Consider the 1END card of the initial zero step:

(1)   The literal 1END in card columns 77-80 remain unchanged.

(2)   Card column "one" of the 1END card contains the value of a variable integer ISIB. If the integer ISIB is zero or blank, the VISCEL program functions in the same manner as the original version, and the additional inputs are never used. If ISIB is defined by a nonzero integer, the new stress link will be activated.

(3)   Card column "two" of the 1END card contains the value of a variable integer ISIP. This variable is used only if ISIB is nonzero. If ISIP is larger than zero, details of the stress computation by the new link will be printed out. If ISIP is set to 1, in addition to the detailed new stress computation printout, the printout of the deflection link (LINK3) will be suppressed, and the execution of the original version of the stress computation (LINK4) will be bypassed. If ISIP is zero or blank, details of the new version of the stress computation will be bypassed. In any case, no further information should be placed on this card.

(4)   If calculations according to the various failure criteria described in Sec. II-B-2 are desired, then an array of data containing positive values of the constants k and S_T for each material of the model must be supplied so that calculations for the generalized Von Mises criterion can be performed. Thus, for each material, two values are needed. These are defined on a set of new cards that contain the same information described in (1), (2), and (3) above. In addition, in fields 3-12 and 13-22, 23-32 and 33-42, and 43-52 and 53-62 these new 1END cards contain values of the pair of material constants k_1 and S_{T1}, k_2 and S_{T2}, and k_3 and S_{T3}, respectively. Only three pairs can be accommodated per card. As many cards are added as required.

(5)   If there is more than one solution step, as in the case with incremental temperature loading in VISCEL, the same rules described in (1) through (4) above apply to each solution step. Values of k and S_T may vary from one solution step to the other. If the failure criteria information described in (4) are needed for a group A of

the solution steps, but need be suppressed for another group B, suppression can be accomplished by leaving blank the values of all the k's and S_T's of item (4) above in the solution steps of group B.

III. APPLICATION TO THE THERMAL STRESSES IN THE N-INTERCONNECT JOINT

An application of the various improvements discussed in Section II-B is demonstrated here by analyzing the thermal stresses induced in the N-interconnect joint in two JPL solar cell design configurations. The two configurations are shown in Figs. 1 and 2, the difference being mainly in the N- and the P-interconnect geometry. These designs were tested previously in the Space Molecular Sink (Ref. 2) in an environment simulating that of Fig. 3. The test results indicated that failure of the N-interconnect joint was the most prevalent failure mechanism, resulting in significant electrical degradation of the solar cell array power output. This failure appeared first as superficial hairline fractures developing between the N-interconnect and the solder joint fillets. The superficial fractures gradually propagated across the entire solder joint as shown in Fig. 4. Subsequent total delamination and further cracking and chipping of the silicon itself were observed in some cases.

The occurrence of such series of events is predicted in the present analysis, not in terms of the number of thermal cycles required to produce each event but in terms of the stress pattern and intensity leading to the development of failure. This latter approach was selected because it proved more reliable and practical than the former. Thus, the distribution of stresses and their magnitude and degree of severity are important output quantities in the present analysis.

The analysis consisted of constructing plane-stress finite element models for the N-interconnect joint of the two configurations in Figs. 1 and 2. Figure 5 shows a portion of one of the models. It includes the 0.0127-cm (0.005-in.) thick Kovar ribbon for the N-interconnect, solder alloy junction (62 Sn, 36 Pb, 2 Ag), 0.0356-cm (0.014 in.) thick silicon wafer, 0.0152-cm (0.006-in.) thick RTV-560 adhesive, and a honeycomb substrate (0.127-cm aluminum core, 0.013-cm-thick aluminum skin on both sides).

The thermal profile of Fig. 3 was simulated in the analysis by five successive thermal increments of 0, -50, -50, -50, and -35°C. Table 1 includes a list of the material properties used for each increment. These were input in the computer program along with other necessary information defining the finite element models according to the rules set forth in Section II-C and Ref. 5.

At the end of each thermal increment, the accumulated values of the stress components σ_x, σ_y, T_{xy} and effective stress σ_{eff} at each of the node points in the models were computed by the procedure reported previously (Ref. 2). In addition, intermaterial boundary stresses were also computed in the new stress link according to Section II-B and Appendix A. These include the accumulated stress components σ_x, σ_y, T_{xy}, satisfying geometric compatibility, force equilibrium and material constitutive relationships implied by the values in Table 1. They also include the failure ratios R_1 and R_2.

By comparing results of the different thermal increments, it was found that all the stress quantities reach their maximum at the lower extreme (-185°C) of the temperature cycle. Figure 6 and Table 2 provide a concise presentation of results relevant to the description of the N-interconnect joint failure mechanism. The most stressed locations in the N-interconnect joint are noted by the labels A_1 through A_{10} in Fig. 6. The corresponding stress ratios are presented in Table 2 for the two configurations of Figs. 1 and 2. Three stress ratios, R_1, R_2, and R, are given for each configuration. These are computed as described in Section II-B: R_1 for the maximum shear stress criterion and R_2 for the generalized Von Mises criterion for materials having different strength values in tension from that in compression. The third ratio, R, is included for comparison only. It was calculated by the conventional procedure of Ref. 2, using the unmodified version of VISCEL. For the reasons discussed in Section II, R_1 and R_2 values should be regarded as more accurate over values of R.

In comparing values of R_1, R_2, and R, it is noted that values of R are either smaller or equal to R_2 and, on the average, R_1 values are about 10% higher than R_2. Thus, for design purposes, R_1 values give a more conservative estimate of the failure condition. R_1 values, which are based on the maximum shear stress criterion, are suitable for failure prediction in ductile metals. Consequently, description of failure in the Kovar and solder, locations A_1 through A_7, are based on R_1. On the other hand, failure by brittle fracture is most likely to occur in the silicon and silicone adhesives at the lower extreme (-185°C) of the temperature cycle. For these conditions, R_2 values, which are based on the generalized Von Mises criterion, should predict failure more accurately at locations A_8 and A_9 in the silicon and A_{10} in the RTV-560 silicone adhesive. In this manner, the combinations of R_1 and R_2 denoted by asterisks in Table 2 are used below.

In theory, failure emerges at a given location when the failure ratio there reaches unity. Failure ratios above unity are interpreted as indicating that failure at the location in question has already begun at a prior temperature level. In this sense, higher failure ratios are indicative of more severe stress concentration. Thus, by comparing the failure ratios of various locations within the first configuration, it is evident from Table 2 that a ductile failure in the solder at A_5, followed by a brittle fracture in the silicon at A_8 and subsequent total separation in the solder junction at A_6 and A_7, are a most likely order of events. The occurrence of the same series of events is also suggested with some variance by the failure ratios of the second configuration. In terms of its overall performance, the second configuration seems to have some advantages over the first. This is suggested by the general tendency toward a lower and less emphatic distribution of the failure ratios in the second configuration over the first.

In the present example, two solar cell configurations compatible with rigid substrates were examined. As other designs compatible with the more flexible lightweight substrates become available, their material selection, design optimization, and failure prediction can be performed by the same procedure described above. This requires, however, a knowledge of the behavior of the thermomechanical properties of all materials involved. Most of the needed information is available in Ref. 2 for several solar cell materials. Additional materials of importance to lightweight solar cell array designs are investigated in the next section.

IV. MATERIAL PROPERTIES

The thermal and mechanical properties of the solar array components elucidated in Ref. 2 are extended herein for additional materials of special importance in the design of lightweight solar cell arrays. These include the filter glass material microsheet-0211 and five candidate materials for the substrate: Kapton-H, Kapton-F, Teflon, Tedlar, and Mica Ply PG-402. Thermomechanical properties required for calculating the stresses resulting from thermal cycling are the coefficient of thermal expansion, elastic moduli, Poisson's ratio, and failure stresses. Because most of the candidate materials considered are nonstructural, there exists a paucity of information in the literature concerning their mechanical properties, especially at low temperatures.

To obtain the needed data, thermal and mechanical characteristic tests were conducted at temperatures in the range -200 to +200°C on thin sheets of the candidate materials. The resulting test data are presented next.

A. MICROSHEET-0211 FILTER GLASS MATERIAL

Annealed bulk specimens of solar cell cover glass were obtained and their thermal and mechanical properties tested. In addition to the coefficient of thermal expansion, measurements of the elastic modulus E, shear modulus G, and Poisson's ratio μ were performed from approximately -200 to +200°C.

1. Instantaneous Coefficient of Thermal Expansion

The thermal expansion coefficients were derived from measurements of the microsheet-0211 filter glass length variation with temperature. The initial approximate dimensions of the specimens were 0.0051 cm thick and 10.0 cm in length at +25°C. The test apparatus used a special vitreous silica dilatometer of the ASTM E-228.

The specimens were first cooled to approximately -200°C; then measurements of the change in length, ΔL, were obtained at progressively higher temperature increments of ~25°C until the upper limit of +200°C was reached. Measurements below room temperature utilized a linear differential transformer as an extensometer; above room temperature a calibrated dial gage was used. Liquid nitrogen was used for the initial cooling and a furnace for the subsequent temperature increases.

With the temperature +25°C as reference, the fractional length $\Delta L/L_0$ was found to vary from -0.1138% at the low temperature limit to +0.1244% at the high temperature. From the data on the variation of the fractional length, $\Delta L/L_0$, the "instantaneous" coefficient of linear thermal expansion α_i was computed by forming the ratio:

$$\alpha_i = \frac{(\Delta L/L_0)_2 - (\Delta L/L_0)_1}{T_2 - T_1} = \frac{L_2 - L_1}{L_0(T_2 - T_1)} \tag{3}$$

in which the subscripts 1 and 2 refer to measurements of any two successive increments, while the subscript 0 refers to measurements at the reference temperature of 25°C. In contrast with the conventional "mean" coefficient of linear thermal expansion α_m given by

$$\alpha_m = \frac{L_2 - L_0}{L_0(T_2 - T_0)} \quad , \tag{4}$$

the instantaneous coefficient is a more accurate representation of the material's dimensional changes away from the reference temperature. In addition, it is better suited for the stress calculation due to incremental thermal disturbances. In Fig. 7, the instantaneous coefficient of thermal expansion is plotted vs temperature for the microsheet-0211 material. The curve increases monotonically; it shows the most well-behaved thermal property of any of the materials investigated. No molecular transitions were observed.

2.   Elastic Moduli and Poisson's Ratio

Measurements of the modulus of elasticity E and shear modulus G for the microsheet-0211 glass were performed in the temperature range -192 to +199°C at increments of about 25°C. The test procedure employed is that of the ASTM-C623, in which the modulus of elasticity is evaluated indirectly by measuring the first and second bending frequencies of a rectangular bar specimen. Similarly, the shear modulus is evaluated indirectly by measuring the fundamental torsional frequency of the rectangular bar specimen. Once the elasticity modulus and the shear modulus are known, the corresponding Poisson's ratio can be computed from the relationship $\mu = [(E/2G)-1]$. Depending on the tolerances of the specimen dimensions and frequency measuring accuracy, it is possible to maintain an accuracy on the order of 1% for moduli and 10% for Poisson's ratio. The average sample dimensions of specimens were 13.035 cm × 2.016 cm × 0.254 cm.

Figure 8 shows the test results of the elasticity modulus variation with temperature. The E_1 values correspond to the first bending frequency measurements; the E_2 correspond to the second bending frequency. A tendency toward a decrease in the modulus values with an increase in temperature above 50°C is exhibited by values of E_1. The same trend is clear from Fig. 9 for the shear modulus G. Poisson's ratio values μ, corresponding to E_1 and G, are given by Fig. 10. They are almost independent of temperature. For design and analysis purposes, the dotted curves are recommended.

B.   SUBSTRATE MATERIALS

In addition to the microsheet-0211 for solar cell filter material, the following five materials for the solar cell substrate were investigated.

(1)   Tedlar (a polyvinyl fluoride film).

(2)   Teflon (a fluorinated ethylene propylene film).

(3)   Kapton-F (a Kapton-H/Teflon laminate).

(4)   Kapton-H (a polyimide).

(5)   Mica Ply (PG-402) (a fiberglass/polyimide composite).

The first four of the five materials tested were long chain polymers. Information regarding their composition and characteristics is given in Appendix B. Tedlar consisted of 0.0051-cm (0.002-in.) thick polyvinyl fluoride; the Teflon specimen was 0.0127 cm (0.005 in.) thick. Also, Kapton-H consisted of 0.0076 cm (0.003 in.) polyimide film. On the other hand, the Mica Ply is made from polyimide resin and a single ply of 1080 fiberglass fabric of 0.0064 cm (0.0025 in.) thickness. Kapton-F was a laminated film consisting of a 0.0051-cm (0.002-in.) thick Kapton-H layer sandwiched between two Teflon layers, each 0.00127 cm (0.0005 in.) thick. The above thicknesses for the test specimens were chosen as close as possible to those expected for the solar cell substrate. This should allow greater relevance and higher confidence in the test results of properties that depend on the specimen dimensions, such as the tensile and compressive strength, and quantities associated with the material's behavior at failure.

Included in the property investigation for each of the five materials are the instantaneous coefficient of thermal expansion, Poisson's ratio, the elastic modulus, yield stress when a yield point is defined, and the stress-strain relationships up to the fracture point. The test measurements of these properties were made at several temperatures in the range -200 to +200°C.

1.   Instantaneous Coefficient of Thermal Expansion

The test specimens used for this purpose were typically 9.398 cm (3.7 in.) long with a maximum thickness of 0.229 cm (0.090 in.) and a width of 2.29 cm (0.9 in.). A brief description of the test instrument and its special features is given in Appendix C. As in the previous glass measurements, the data recorded during the test consisted of the change in the specimen length ΔL at increments of ~25°C. The temperature of the test chamber was adjusted prior to recording the data until the temperature of the test specimen reached equilibrium. The accuracy of measurement is estimated at $\pm 5 \times 10^{-5}$ cm/cm over the full temperature range. Using the same procedure of Section IV-A, the instantaneous coefficient of linear thermal expansion was computed and plotted as shown in Figs. 11 through 14.

Teflon was not included in the thermal expansion test program. Its instantaneous coefficient of linear thermal expansion α_i was computed approximately from data on the mean coefficient of linear thermal expansion α_m given in Ref. 6. This was done by using Eq. (4) for α_m to compute $\Delta L/L$ for successive temperature increments, then using Eq. (3) to compute corresponding values for the instantaneous coefficient α_i. The results obtained in this manner are shown in Fig. 15 in addition to results given in Ref. 7. Despite the approximate nature of the computation, both results agree very well. The presence of a transition phase in the vicinity of room temperature is clearly defined in both results. Tedlar, Fig. 11, exhibited a similar transition slightly above room temperature. In the remaining materials, Kapton-F and Kapton-H (Figs. 12 and 13), no strong transition was detected from the data. Kapton-H showed more variation at the measured points than Kapton-F (1 mil Kapton H polyimide with 0.5 mil Teflon-FEP facings). Very few points were taken in the transition

region, 20 to 30°C, for Kapton-F. However, at the low temperature the increasing slope of the curve is similar to that of the Teflon-TFE coefficient of thermal expansion data (Fig. 15). The second-order crystalline transitions of Teflon are not observed in the Kapton-F data because the FEP type Teflon does not undergo these transitions in this temperature range (Ref. 6).

2. Poisson's Ratio

The test setup and procedure used for Poisson's ratio measurement and all the remaining mechanical properties are described in Appendix D. In the performance of these tests, certain improvements and special techniques were developed. For example, a special gripping and clamping procedure was developed to insure uniformity of the loads applied to the specimens. Also, because the test specimens are very thin films, Poisson's ratio measurements using conventional strain gauges resulted in considerable errors. The errors arise from the fact that the gauge stiffness is comparable to the specimen stiffness. Thus, to facilitate Poisson's ratio measurements, fiducial cross patterns were inked on the surface of each specimen and subsequently photographed as they deformed under loading. The relative lateral to longitudinal deformations of the central part of each specimen provided a measure of Poisson's ratio.

In spite of the precautions mentioned, as much as ±35% scatter in Poisson's ratio values was observed, especially at higher temperatures. A possible reason for this could be because these materials have a very narrow initial elastic range, requiring very small loads and strains, and hence resulting in greater experimental errors.

Even with these limitations, it is possible to draw some conclusions about the nature and variational trend of the average values of Poisson's ratio for the five substrate materials as temperature was changed. Figure 16 shows these average values. In the higher temperature range, 100 to 200°C, the average values of Poisson's ratio are seen to fall between 0.39 and 0.51. The spread in values became greater near room temperature, then diminished to between 0.26 and 0.42 near -195°C. The greater spread in values around room temperature could be related to the transition phases revealed in much stronger terms in the instantaneous coefficient of thermal expansion data of Figs. 11-15. Generally, in the temperature range -200 to +200°C, Poisson's ratio values tended to be higher at the higher temperature end and lower at the lower temperature end, with some variations in between the two extremes. Of all the five substrates tested, only Kapton-H showed relatively uniform progression in values as the test temperature was changed from -195 to +200°C.

Little information is available in the literature concerning the temperature effects on Poisson's ratio for polymers. Reference 8 gives a value of 0.38 for polyethylene, presumably at room temperature. This shows good agreement with Kapton-H. The general increase in the values toward 0.5 (like rubber and liquids at 0.49) as the temperature is raised reflects the general decoupling of the long-chain molecules. The more rigid polymers such as polystyrene and polymethyl methacrylate have a lower Poisson's ratio 0.33 (Ref. 8).

Therefore, it appears that, with increasing temperature, changes in the crystalline structure occur that permit the morphology of the polymer to become

more liquidlike. The microscopic changes involved can be quite complex (Ref. 9), but the net result is greater elasticity of the structure.

3. Elastic Modulus

The test setup of Appendix D was used in determining the elastic modulus values for each of the five substrate materials at six different temperatures: -195, -100, -25, +25, +100, and +200°C. Air was used for heating the test chamber above room temperature. Cooling the test chamber presented special difficulties.

It has been shown (Refs. 10, 11) that some polymers craze in the presence of carbon dioxide, argon, or nitrogen, when the temperature approaches the boiling point of the cooling medium.[2] At that temperature, the cooling medium tends to diffuse into the polymer. In general, stress concentrations in the polymer specimen produce conditions favorable to craze nucleation by creating local cavities. The depth of diffusion into the polymer, although stress-dependent, is usually shallow and affects properties such as the yield and fracture strength, which are functions of the surface condition. For thin polymer films, as is the case here where thicknesses vary from 0.0051 to 0.0254 cm, the depth of surface diffusion accounts for a sizable percentage of the film thickness. Under these conditions, it is reasonable to expect such properties as the elastic modulus, whose values normally depend only on conditions of the bulk, to depend as well on diffusion of the cooling medium into the surface. This conclusion is supported by the dramatic reduction of approximately 50% in the elastic modulus values of Teflon at -25°C (Table 3), when the cooling medium is carbon dioxide as compared to nitrogen. Other properties listed in the table for Teflon and Kapton-H emphasize the adverse effects of the cooling medium and the possible engineering hazards involved in a frequently indiscriminate choice of the cooling medium for thermal cycle testing of solar cell arrays or their components. In the results of Table 3 and all subsequent tests for the substrate materials, nitrogen did not show anomalies that are characteristic of crazing and was therefore used as refrigerant.

Elastic modulus measurements were made from the initial slope of the load-extension chart produced by the Instron machine. There, the specimen extension is measured by the relative displacement between the load cell and the cross head. Specimen gauge length of 10 in. is recommended by the ASTM test procedure. However, because of the high ductility of some of these polymers, especially above room temperature, and because of the limited amount of travel allowed in the test chamber, shorter gauge length had to be used.

Table 4 lists the elastic modulus values resulting from 2.54-cm (1-in.) 10.16-cm (4-in.), and 20.32-cm (8-in.) gauge lengths. The shorter the gauge length, the smaller the measured elastic modulus value. Because a true elastic modulus value should not depend on the specimen dimensions or geometry, the results of Table 4 are indicative of test errors that must be corrected. The possibility that the errors could have resulted from too high cross head speed was investigated and subsequently rejected. Instead, these errors

---

[2]No crazing was reported when helium or vacuum was used.

are believed to have resulted from a combination of (1) extensions in the grip and linkages of parts of the machine near the cross head, and (2) additional nonuniform extension and possible slippage of the wrapped-around portion of the specimen. Both effects contribute to greater errors for shorter specimens.

A correction to these errors was implemented by making use of the photographic technique for the longitudinal strain measurements. As in the case for Poisson's ratio measurements, strains were computed from the longitudinal deformations of a central portion of the specimen, away from the ends and excluding their influence. Correction factors were computed by comparing the extension obtained from the displacement between the cross head and load cell, with the extension determined from photographs of the fiducial patterns. The correction factors were computed at various temperatures and applied to the corresponding results presented below.

A partial check was made at room temperature by deriving the corrections by a different approach. This latter approach is based on the premise that the true elastic modulus should be independent of the specimen gauge length. Thus, if the measured "apparent" elastic modulus values are plotted against the gauge length, as shown in Fig. 17, the "true" elastic modulus should be given by a line parallel to the gauge length axis and asymptotic to the curves at the greater gauge length. This is true because greater errors are associated with shorter specimens. The corrected elastic moduli for room temperature resulting from the first approach and based upon extrapolation of the curves are compared in Fig. 17. The corrected elastic moduli obtained by the two approaches are in relatively good agreement.

In Tables 5 through 9, the measured and corrected values of elastic moduli are given for each of the five substrate materials at various temperatures for the machine and the transverse direction of the specimens. The difference between the machine and transverse direction properties is indicative of the degree of orthotropy of these polymers. The Mica Ply PG-402 composite exhibited the greatest orthotropy of all the five materials tested. The transverse (fill) direction moduli for the Mica Ply are consistently about 75% of those in the machine (warp) direction.

The temperature-dependence of the elastic modulus values is depicted in Figs. 18 and 19. The rate of change of these moduli with temperature varied greatly for each material at different temperatures. In addition, Kapton-H showed some degree of irregularity at room temperature. These irregularities are characteristic of the behavior of the mechanical properties of long-chain polymers (Ref. 8). They result from many types of transitions that can occur at different temperatures, including crystal melting, first-order crystalline transitions, glass transitions, and secondary glass transitions.

4.   Stress-Strain Behavior, Yield Stress, and Fracture Strength

The stress-strain curves[3] up to fracture were determined for each of the five materials at each of the six temperatures, namely -195, -100, -25, +25,

---

[3]Effects of strain rate and time on the creep and viscous flow when loads are sustained for long times are not considered.

+100 and +200°C. Many of the special procedures and treatments discussed in the previous two sections and in the appendixes were used here. Typical tensile stress-strain curves at each of the test temperatures are shown in Figs. 20 through 24 for Kapton-H, Kapton-F, Teflon, Tedlar, and Mica Ply PG-402. The significance of these curves is mainly qualitative, showing trends and characteristics of the material behavior under stress and temperature and thus providing important design information.

Depending on the temperature and material, the initial linear elastic region constituted from 0 to 100% of the total range to failure. For example, Teflon and Tedlar (Figs. 22 and 23) behaved completely inelastically above 100°C, but almost completely elastically and linearly near -195°C. Except for a limited initial linearity, Kapton-H and Kapton-F (Figs. 20 and 21) tend to behave markedly nonlinearly under loads at almost all temperatures within the range in question. Mica Ply PG-402 on the other hand, responded linearly to loads at all temperatures investigated because of the fiberglass reinforcement (Fig. 24).

Yielding in polymeric materials may take place by various mechanisms. These include slipping between molecules or chains of molecules. Molecular bonds may be temporarily broken and then reformed, or they may be permanently broken. Friction, interlocking between particles, or fragmentation of particles are possible. The question as to which of these mechanisms or combination of mechanisms will actually take place depends upon, among other things, the chemical composition, temperature, history of loading, and degree of crystallinity. Accordingly, yielding may occur on a continuous and gradual basis, as is the case with Kapton-H and Kapton-F at all temperatures investigated (Figs. 20 and 21). By contrast, yielding may occur at a definite stress level as exhibited by Teflon and Tedlar at temperatures below +25°C (Figs. 22 and 23) and by Mica Ply PG-402 (Fig. 24) at almost all temperatures. Here again, the absence of a definite yield point in Tedlar and Teflon above +25°C and the presence of a rather distinguishable one below that temperature indicate a strong association with the same transformation revealed in the data on the thermal coefficient of expansion (Fig. 15).

In testing of the five materials, a 3% offset yield stress was used to define the yield point when a distinguishable yield point was not present. While Figs. 20 through 24 represent the stress-strain curves for selected, but typical, single test specimens, Figs. 25 and 26 depict the variation of the statistical average yield stress of all specimens as temperature is changed from -200 to +200°C. As may be expected, higher yield stresses are associated with lower temperatures.

There are other very important design quantities such as the fracture stress and strain that can be derived from the stress-strain behavior. Because fracture failures in general are very sensitive to the presence of local imperfections and the magnitude of the stress concentration at imperfections, the fracture strength can be meaningful only in a statistical sense. This is especially true for a brittle material like the Mica Ply PG-402 at nearly all temperatures (Figs. 27 and 28). The specially designed cutting procedure of Appendix E was intended to minimize the presence of edge imperfection and stress raiser as much as possible. The results evidenced by the microscopic examination of these edges (Appendix E) were smooth and relatively free from imperfection except in the case of Mica Ply PG-402. This explains the reason for the greater deviation from the average values in the case of Mica Ply

fracture stress data (Fig. 28). In Figs. 27 and 28 the average fracture stress values are plotted against temperature, with the vertical bars representing the magnitude of the standard deviations when the deviation was large.

In analogy to the fracture stress variation with temperature, Fig. 29 shows the relationship between the test temperature and the total strain accumulated up to fracture. The magnitude of these strains is a measure of brittleness or ductility of the material. The four materials included in Fig. 29 behaved in a brittle fashion near -200°C, but became increasingly ductile as temperature was increased. Note that in the case of Teflon and Tedlar, the maximum fracture strains were reached between 75 and 125°C, rather than at 200°C. The reasons may be that the mechanism of deforming these materials and the mechanism of their fracture are different and have different temperature-dependence. Deformation is accomplished by stretching, uncoiling, or breaking of molecular chains in localized internal areas, while fracture is a gross rupture of the molecular structure, usually starting at an edge flaw or a surface crack.

According to Fig. 29, Teflon exhibited the greatest ductility of all the materials at temperatures above -25°C. It is followed by Tedlar, Kapton-F, Kapton-H, then by Mica Ply PG-402. The latter was not included in the figure because it had very low ductility. As a composite material, the Mica Ply generally showed different behavioral patterns from the remaining four polymeric materials.

V. DISCUSSION AND CONCLUSIONS

Investigation of thermal stresses in solar cell arrays, a seemingly unimportant subject for the photovoltaic specialist and a routine exercise for the material and stress analyst, has contributed to the understanding of reasons for mechanical failures and subsequent power degradation of solar cell arrays. This was demonstrated here by an example in which the stress distribution in the N-interconnect junction of certain JPL solar cell designs was examined when large thermal changes were involved. Improved material characteristics contributed to the success of this approach.

To accurately compute these stresses, improvements were introduced in the conventional procedure for stress computation in the displacement-based finite element approach. In a usual structural problem, errors in the stresses computed by the conventional procedures are often within reasonable accuracy because variations in the mechanical properties of the various structural elements are relatively small. Only when one considers the easily deformable materials, such as the adhesives, in contrast with the relatively rigid silicon material do errors accumulate rapidly, thereby requiring the introduced corrections in the stress computation. In the present analysis, accumulated stresses are computed to correspond to temperature increments, the magnitude of which can be arbitrarily selected to account for large or small rates of material property changes with temperature. Thus, when there is a slight change with temperatures in the material properties, it is possible to save on the calculation time without sacrificing accuracy by applying large thermal increments. On the other hand, when the materials go through a phase transition with associated rapid property changes, a very small thermal increment must be used in order to maintain the needed accuracy.

In any case, the computed stresses have additional significance when interpreted in terms of a valid failure criterion. Here again, because of the wide range of behavior of materials involved in the composite solar cell array, it was necessary to provide the solar cell designer with more flexibility in selecting the failure criterion that best describes the failure mode of each material and temperature. The most general criterion covering a wide range of ductile and brittle failure modes is the generalized Von Mises criterion (Section III). It is particularly suitable for predicting failures in the silicon material and adhesives below their glass transition temperature.

The final results presented in Table 2 combine effects of both the stress corrections and the more accurate failure criteria. These are marked with asterisks and are associated with either R_1 or R_2. When compared with the corresponding failure ratios R based on the original version of Ref. 2, the recommended ratios are found to be from 10 to 400% greater in absolute value over R. However, the distribution of areas of relative stress concentration and therefore the order of failure pattern remained unchanged regardless of whether R, R_1, or R_2 was used. This is a peculiarity of the current example and should not be expected as a general rule.

None of the above stress and failure analyses could be performed without a good understanding and a reasonably accurate description of how certain key properties of the solar cell materials change with temperature. For this purpose, original work was carried out to identify the temperature-dependence of selected materials of importance to the design of lightweight solar cell arrays. They are the microsheet-0211 glass material for solar cell filter, along with five substrate materials: Kapton-H, Kapton-F, Teflon, Tedlar and Mica Ply PG-402. The temperature-dependence of the coefficient of thermal expansion, elastic moduli, Poisson's ratio, strain and stress behavior of these materials up to failure were determined. The properties were determined to different levels of accuracy, depending on the composition of the individual material, its stability in thermal environment, and the suitability of the employed test technique. Properties of the microsheet-0211 glass material were relatively well-behaved. On the other hand, properties of the Mica Ply PG-402 were rather ill-behaved, primarily because it is a two-phase material in which the fibers are not adequately stabilized to achieve consistent strength.

Most of the polymeric materials for the substrate showed strong, and occasionally abrupt, changes with temperature. These result from many types of phase transitions that can take place at different temperatures. Crystal melting, first-order crystalline transitions, glass transitions, and secondary glass transitions are possible causes. For the purpose of the present work, it is not as important to identify which of these transitions actually took place as it is to determine their net effect, whenever possible. A full investigation of this subject was not attempted here because it requires much more elaborate test techniques and greater cost. However, several of these effects were observed and recorded in connection with a number of the material properties in question.

When thermal cycling tests of solar cell arrays are performed, a judicious selection of the cooling medium is of prime importance. As was pointed out in Section IV-B-3, certain refrigerants tend to easily diffuse into certain polymers when their boiling point is reached. If this occurs, anomalous effects and premature failures can result. Unless this is known, erroneous results may go unnoticed.

Table 1. Material properties used in the analysis (Ref. 2)

Thermal increment,[a] °C	Material[b]	Elastic modulus, MN/cm^2 (10^6 psi)	Shear modulus, MN/cm^2 (10^6 psi)	Instant coefficient of expansion $\times 10^{-6}$/°C ($\times 10^{-6}$/°F)	k (Section II-B-2)	S_T (Section II-B-2), kN/cm^2 kpsi
	1	13.10 (19.00)	4.90 (7.10)	6.50 (3.61)		
	2	2.41 (3.50)	0.85 (1.24)	22.0 (12.2)		
0	3	12.41 (18.00)	4.85 (7.03)	2.00 (1.11)		
	4	1.59 (2.30)	0.54 (0.78)	225.0 (125)		
	5	0.083 (0.121)	0.031 (0.045)	22.0 (12.2)		
	1	13.10 (19.00)	4.90 (7.10)	6.50 (3.61)	1.0	62.05 (90.0)
	2	2.41 (3.50)	0.85 (1.24)	22.0 (12.2)	1.0	6.89 (10.0)
-50	3	12.41 (18.00)	4.85 (7.03)	2.00 (1.11)	7.0	20.68 (30.0)
	4	1.59 (2.30)	0.54 (0.78)	225.0 (125)	1.0	0.689 (1.0)
	5	0.083 (0.121)	0.031 (0.045)	22.0 (12.2)	1.0	27.58 (40.0)
	1	13.10 (19.00)	4.83 (7.00)	6.50 (3.61)	1.0	68.95 (100)
	2	3.79 (5.50)	1.35 (1.96)	21.0 (11.67)	1.0	11.02 (16.0)
-50	3	12.41 (18.0)	4.83 (7.00)	1.30 (0.72)	7.0	20.68 (30.0)
	4	2.21 (3.20)	0.89 (1.29)	200 (111.1)	1.0	1.38 (2.0)
	5	0.087 (0.126)	0.032 (0.047)	19.5 (10.8)	1.0	27.58 (40.0)

Table 1 (contd)

Thermal increment,[a] °C	Material[b]	Elastic modulus, MN/cm^2 (10^6 psi)	Shear modulus, MN/cm^2 (10^6 psi)	Instant coefficient of expansion, ×10^{-6}/°C (×10^{-6}/°F)	k (Section II-B-2)	S_T (Section II-B-2), kN/cm^2 kpsi
-50	1	13.03 (18.9)	4.76 (6.90)	6.50 (3.61)	1.0	89.63 (130)
	2	4.48 (6.50)	1.60 (2.32)	18.0 (10.0)	1.0	13.79 (20.0)
	3	12.41 (18.0)	4.81 (6.98)	0.20 (0.11)	7.0	20.68 (30.0)
	4	1.38 (2.00)	0.62 (0.90)	110. (61.11)	1.5	3.10 (4.5)
	5	0.092 (0.134)	0.034 (0.050)	16.5 (9.17)	1.0	27.58 (40.0)
-35	1	12.96 (18.8)	4.76 (6.90)	6.50 (3.61)	1.0	110.3 (160)
	2	4.83 (7.00)	1.73 (2.51)	16.0 (8.89)	1.0	17.24 (25.0)
	3	12.41 (18.0)	4.81 (6.97)	-0.90 (-0.5)	7.0	20.68 (30.0)
	4	1.03 (1.50)	.469 (0.68)	30.0 (16.67)	5.0	4.14 (6.00)
	5	0.099 (0.143)	0.037 (0.054)	11.0 (6.11)	1.0	27.58 (40.0)

[a]First zero thermal increment is necessary for initialization only. Its properties are arbitrary since it produces no stresses.

[b]Material type 1 = Kovar, 2 = solder, 3 = silicon, 4 = RTV-560 adhesive, 5 = equivalent solid aluminum substrate.

Table 2. Summary of failure ratios in N-interconnect junction

Config-uration	Fail-ure ratio	Location designated in Fig. 6b									
		A_1	A_2	A_3	A_4	A_5	A_6	A_7	A_8	A_9	A_{10}
1	R_1	0.12*	0.50*	0.30*	0.28*	2.3*	0.62*	0.75*	–	–	–
	R_2	0.10	0.44	0.275	0.26	2.0	0.57	0.65	1.2*	0.46*	0.28*
	R	0.10	0.27	0.275	0.19	2.0	0.25	0.40	0.31	0.33	0.30
2	R_1	0.33*	0.31*	0.31*	0.26*	1.8*	0.61*	0.64*	–	–	–
	R_2	0.03	0.28	0.275	0.25	1.6	0.55	0.59	1.5*	0.79*	0.56*
	R	0.03	0.125	0.275	0.105	1.6	0.32	0.48	0.38	0.12	0.22

Table 3. Effects of testing in carbon dioxide and nitrogen
(2.54-cm gauge length, machine direction, -25°C)

Material	Measured elastic modulus, GN/m^2 (psi)	3% yield stress, MN/m^2 (psi)	Fracture stress, MN/m^2 (psi)	Fracture strain, %	Refrigerant
Teflon	0.41 (59,600)	22.48 (3,260)	44.13 (6,400)	505	CO_2
Teflon	0.89 (129,290)	18.96 (2,750)	31.23 (4,530)	303	N_2
Kapton-H	1.34 (194,890)	55.85 (8,100)	111.35 (16,150)	66	CO_2
Kapton-H	2.04 (295,710)	71.29 (10,340)	161.96 (23,490)	96	N_2

Table 4. Effects of gauge length
(25°C, machine direction)

Material	Elastic modulus, GN/m^2 (psi)	3% yield stress, MN/m^2 (psi)	Fracture stress, MN/m^2 (psi)	Fracture strain, %	Gauge length, cm (in.)
Kapton-H	3.66 (531,110)	108.11 (15,680)	179.13 (25,980)	35	20.32 (8)
	2.94 (426,820)	97.56 (14,150)	199.53 (28,940)	58	10.16 (4)
	2.23 (323,280)	101.39 (14,705)	210.56 (30,540)	71	2.54 (1)
Kapton-F	2.53 (366,670)	68.40 (9,920)	142.65 (20,690)	81	20.32 (8)
	1.95 (282,850)	62.26 (9,030)	132.66 (19,240)	73	10.16 (4)
	1.44 (208,190)	63.98 (9,280)	134.45 (19,500)	90	2.54 (1)
Teflon	0.47 (68,410)	13.44 (1,950)	24.68 (3,580)	351	20.32 (8)
	0.43 (63,060)	9.93 (1,440)	17.86 (2,590)	295	10.16 (4)
	0.34 (48,710)	12.20 (1,770)	18.27 (2,650)	317	2.54 (1)
Tedlar	1.74 (251,900)	38.06 (5,520)	75.43 (10,940)	150	20.32 (8)
	1.50 (217,870)	32.27 (4,680)	72.74 (10,550)	164	10.16 (4)
	1.18 (170,780)	35.16 (5,100)	79.98 (11,600)	224	2.54 (1)
PG-402	12.16 (1,763,900)	- -	170.44 (24,720)	2	10.16 (4)
	5.70 (826,000)	184.64 (26,780)	184.64 (26,780)	3.4	2.54 (1)

Table 5. Summary data, Kapton-H
(0.00762 cm, 0.003 in. thick; 2.54 cm, 1.0 in. gauge length)

Test temperature, °C	Measured elastic modulus, GN/m² (psi)	Corrected elastic modulus, GN/m² (psi)	3% yield stress, MN/m² (psi)	Fracture stress, MN/m² (psi)	Fracture strain, %	Specimen direction
200	1.206 (175,050)	1.218 (176,840)	80.96 (11,750)	125.98 (18,285)	83	Machine
200	1.213 (176,040)	1.225 (177,800)	74.34 (10,790)	120.40 (17,475)	79	Transverse
100	2.093 (303,800)	3.621 (526,330)	93.77 (13,510)	161.78 (23,480)	65	Machine
100	1.811 (262,820)	3.133 (454,680)	79.44 (11,530)	153.85 (22,330)	74	Transverse
25	2.227 (323,280)	3.585 (520,500)	101.32 (14,705)	210.42 (30,540)	71	Machine
25	2.218 (321,970)	3.571 (518,370)	98.94 (14,360)	208.09 (30,200)	73	Transverse
-25	3.025 (439,040)	4.507 (654,170)	118.30 (17,170)	237.08 (34,410)	54	Machine
-25	3.009 (436,710)	4.483 (650,700)	116.58 (16,920)	232.33 (33,720)	58	Transverse
-100	3.678 (533,830)	4.781 (693,980)	174.18 (25,280)	313.01 (45,430)	52	Machine
-100	3.648 (529,430)	4.742 (688,300)	159.23 (23,110)	270.29 (39,230)	41	Transverse
-195	4.346 (630,730)	5.215 (756,900)	234.05 (33,970)	350.49 (50,870)	36	Machine
-195	4.168 (604,980)	5.002 (735,300)	225.99 (32,800)	317.15 (46,030)	31	Transverse

Table 6. Summary data, Kapton-F
(0.00762 cm, 0.003 in. thick; 2.54 cm, 1.0 in. gauge length)

Test temperature, °C	Measured elastic modulus, GN/m² (psi)	Corrected elastic modulus, GN/m² (psi)	3% yield stress, MN/m² (psi)	Fracture stress, MN/m² (psi)	Fracture strain, %	Specimen direction
200	0.662 (96,140)	0.715 (103,800)	48.64 (7,060)	88.95 (12,910)	161	Machine
200	0.658 (95,500)	0.711 (103,100)	50.30 (7,300)	87.50 (12,700)	103	Transverse
100	1.354 (196,530)	1.801 (261,400)	55.67 (8,080)	109.07 (15,830)	100	Machine
100	1.421 (206,210)	1.890 (274,300)	57.32 (8,320)	124.71 (18,100)	97	Transverse
25	1.434 (208,190)	2.165 (314,400)	63.94 (9,280)	134.36 (19,500)	90	Machine
25	1.450 (210,440)	2.190 (317,800)	63.04 (9,150)	139.97 (20,315)	72	Transverse
-25	2.037 (295,710)	2.913 (422,900)	71.24 (10,340)	161.85 (23,490)	96	Machine
-25	2.096 (304,150)	2.997 (435,000)	97.29 (14,120)	185.13 (26,870)	77	Transverse
-100	3.110 (451,380)	4.323 (627,100)	129.19 (18,750)	248.87 (36,120)	91	Machine
-100	3.086 (447,960)	4.290 (622,700)	123.81 (17,970)	235.43 (34,170)	70	Transverse
-195	4.778 (693.440)	8.075 (1,171,900)	180.72 (26,230)	310.95 (45,130)	65	Machine
-195	4.603 (668,090)	7.779 (1,128,800)	182.10 (26,430)	327.96 (47,600)	62	Transverse

Table 7. Summary data, Teflon
(0.0127 cm, 0.005 in. thick; 2.54 cm, 1.0 in. gauge length)

Test temp- erature, °C	Measured elastic modulus, GN/m^2 (psi)	Corrected elastic modulus, GN/m^2 (psi)	3% yield stress, MN/m^2 (psi)	Fracture stress, MN/m^2 (psi)	Fracture strain, %	Specimen direction
200	16.71 (2,425)	19.22 (2,790)	1.21 (175)	3.48 (505)	378	Machine
200	15.78 (2,290)	18.15 (2,630)	1.10 (160)	1.93 (280)	298	Transverse
100	55.64 (8,075)	96.81 (14,050)	3.55 (515)	12.33 (1,790)	399	Machine
100	51.05 (7,410)	88.83 (12,900)	2.62 (380)	8.34 (1,210)	324	Transverse
25	335.51 (48,710)	486.49 (70,600)	12.20 (1,770)	18.26 (2,650)	317	Machine
25	346.50 (50,290)	502.43 (72,900)	11.51 (1,670)	17.36 (2,520)	306	Transverse
-25	890.81 (129,290)	1042.25 (150,000)	18.95 (2,750)	31.21 (4,530)	303	Machine
-25	917.82 (133,210)	1073.85 (155,900)	18.53 (2,690)	32.73 (4,750)	314	Transverse
-100	1982.8 (287,780)	2478.5 (348,600)	69.45 (10,080)	67.25 (9,760)	132	Machine
-100	1974.0 (286,500)	2467.5 (358,100)	68.07 (9,880)	66.28 (9,620)	81	Transverse
-195	3290.5 (477,570)	6679.7 (969,500)	98.18 (14,250)	95.01 (13,790)	15	Machine
-195	3553.7 (515,780)	7214.0 (1,047,000)	114.93 (16,680)	109.83 (15,940)	15	Transverse

Table 8. Summary data, Tedlar
(0.0051 cm, 0.002 in. thick; 2.54 cm, 1.0 in. gauge length)

Test temperature, °C	Measured elastic modulus, GN/m² (psi)	Corrected elastic modulus, GN/m² (psi)	3% yield stress, MN/m² (psi)	Fracture stress, MN/m² (psi)	Fracture strain, %	Specimen direction
150	30.66 (4,450)	34.95 (5,070)	3.07 (445)	20.88 (3,030)	238	Machine
150	39.55 (5,740)	45.09 (6,540)	2.84 (412)	18.64 (2,705)	220	Transverse
100	114.20 (16,575)	121.05 (17,570)	7.72 (1,120)	38.72 (5,620)	259	Machine
100	103.97 (15,090)	110.21 (16,000)	6.20 (900)	48.09 (6,980)	224	Transverse
25	1176.7 (170,780)	2388.7 (348,300)	35.14 (5,100)	79.92 (11,600)	224	Machine
25	1152.5 (167,270)	2339.6 (339,560)	32.93 (4,780)	75.24 (10,920)	161	Transverse
-25	1826.7 (265,130)	4146.6 (601,530)	75.51 (10,960)	110.38 (16,020)	129	Machine
-25	1900.0 (275,760)	4313.0 (625,980)	70.14 (10,180)	128.50 (18,650)	102	Transverse
-100	3895.8 (565,430)	8103.3 (1,174,980)	148.76 (21,590)	166.46 (24,160)	38	Machine
-100	4102.7 (595,450)	8533.6 (1,237,340)	154.89 (22,480)	197.40 (28,650)	47	Transverse
-195	4922.4 (714,430)	9401.8 (1,364,550)	213.18 (30,940)	245.28 (35,600)	7.6	Machine
-195	4811.1 (698,280)	9189.2 (1,333,700)	150.89 (21,900)	192.23 (27,900)	7.8	Transverse

Table 9. Summary data, PG-402
(0.00635 cm, 0.0025 in. thick; 2.54 cm, 1.0 in. gauge length)

Test Temp- erature, °C	Measured elastic modulus, GN/m^2 (psi)	Corrected elastic modulus, GN/m^2 (psi)	3% yield stress, MN/m^2 (psi)	Fracture stress, MN/m^2 (psi)	Fracture strain, %	Specimen direction
200	5.428 (787,800)	14.547 (2,111,300)	160.47 (23,290)	160.47 (23,290)	3.2	Warp
200	3.782 (548,870)	10.136 (1,471,000)	103.56 (15,030)	103.56 (15,030)	3.4	Fill
100	5.832 (846,380)	15.222 (2,209,000)	151.10 (21,930)	151.10 (21,930)	2.7	Warp
100	4.342 (630,220)	11.333 (1,644,900)	80.61 (11,700)	80.61 (11,700)	1.7	Fill
25	5.691 (826,000)	19.748 (2,866,300)	184.51 (26,780)	184.51 (26,780)	3.4	Warp
25	4.335 (629,110)	15.042 (2,183,000)	117.68 (17,080)	117.68 (17,080)	2.7	Fill
-25	5.916 (858,640)	19.996 (2,902,200)	171.35 (24,870)	201.81 (29,290)	3.7	Warp
-25	4.372 (634,580)	14.777 (2,144,900)	108.86 (15,800)	131.12 (19,030)	3.8	Fill
-100	6.220 (902,710)	24.071 (3,493,500)	199.33 (28,930)	312.74 (45,390)	6.7	Warp
-100	5.129 (744,360)	19.849 (2,880,700)	104.25 (15,130)	227.85 (33,070)	6.7	Fill
-195	7.431 (1,078,570)	23.036 (3,343,600)	181.41 (26,330)	381.22 (55,330)	7.6	Warp
-195	5.419 (786,480)	16.799 (2,438,100)	131.81 (19,130)	241.91 (35,110)	6.3	Fill

N-INTERCONNECTOR

SERIES

PARALLEL

SOLDER RESIST

P-INTERCONNECTOR

SILICON SOLAR CELL
(2 cm X 2 cm X 0.036 cm)

SILICONE ADHESIVE
(CELL TO COVERSLIDE BOND)

P INTERCONNECTOR

N INTERCONNECTOR

0.051 cm REF

0.01 cm MIN

GLASS
COVERSLIDE

0.127 cm

0.040 cm
RADIUS TYP

SILICON SOLAR CELL
2 cm X 2 cm X 0.036 cm

0.020 cm RADIUS TYP

SILICONE ADHESIVE
(MODULE BOND)

HONEYCOMB SUBSTRATE
1.27 cm CORE (VENTED)
0.013 cm THICK SKIN
BOTH SURFACES

DIELECTRIC INSULATION
0.013 cm FIBERGLASS
EPOXY

Fig. 1. Solar cell configuration 1

N-INTERCONNECTOR

SERIES

PARALLEL

SOLDER RESIST

P-INTERCONNECTOR

N-INTERCONNECTOR

SILICON SOLAR CELL
(2 cm X 2 cm X 0.036 cm)

SILICONE ADHESIVE
(CELL TO COVERSLIDE BOND)

N INTERCONNECTOR

P INTERCONNECTOR

0.051 cm REF

GLASS
COVERSLIDE

0.01 cm MIN

0.127 cm

SILICON SOLAR CELL
2 cm X 2 cm X 0.036 cm

0.046 cm RADIUS TYP

SILICONE ADHESIVE
(MODULE BOND)

HONEYCOMB SUBSTRATE
1.27 cm CORE (VENTED)
0.013 cm THICK SKIN
BOTH SURFACES

DIELECTRIC INSULATION
0.013 cm FIBERGLASS
EPOXY

Fig. 2. Solar cell configuration 2

Fig. 3. Typical solar cell temperature profile during Sun occultation
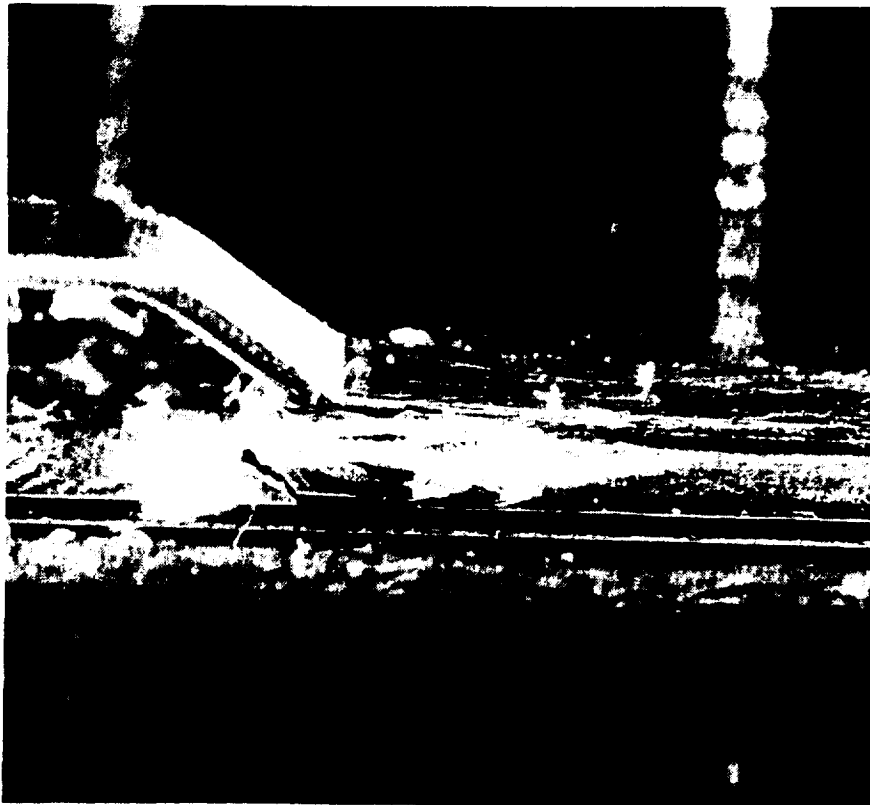
Fig. 4. N-interconnect solder joint failure
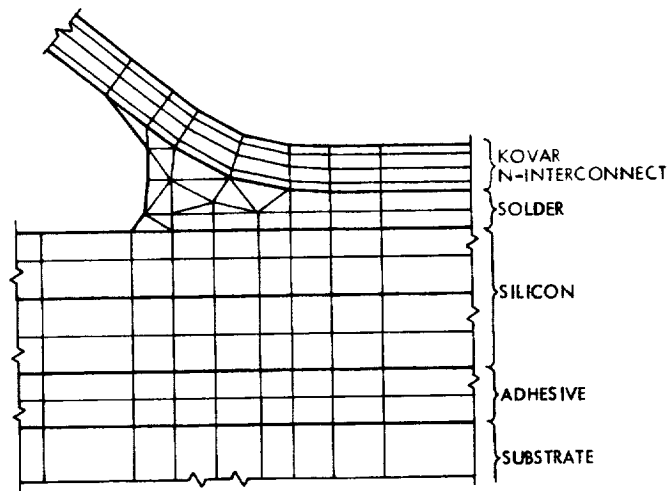
Fig. 5.   Portion of finite element model
of N-interconnect junction
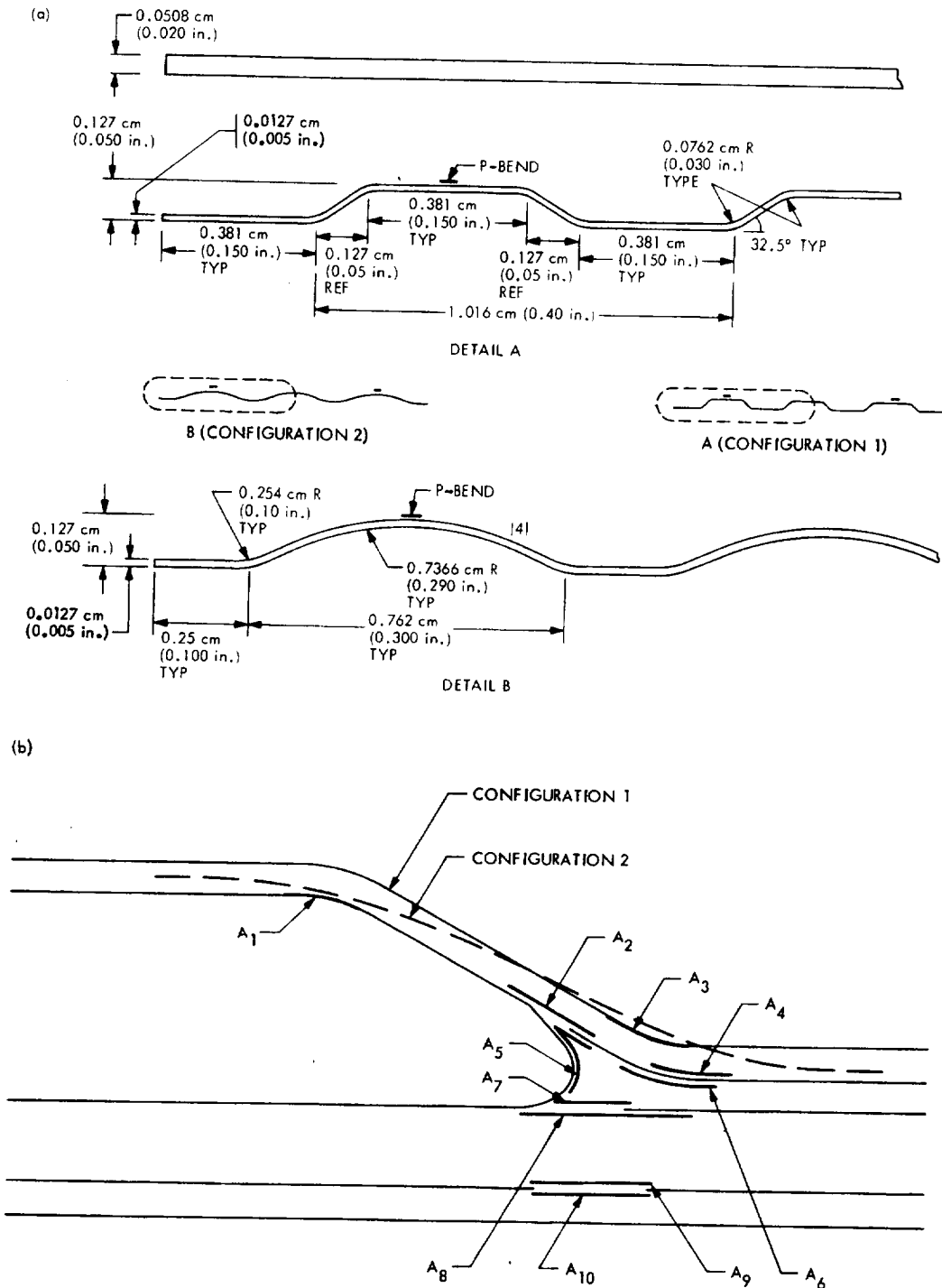
Fig. 6. N-interconnect junction: (a) two interconnect geometries, (b) most stressed areas, leading to failures
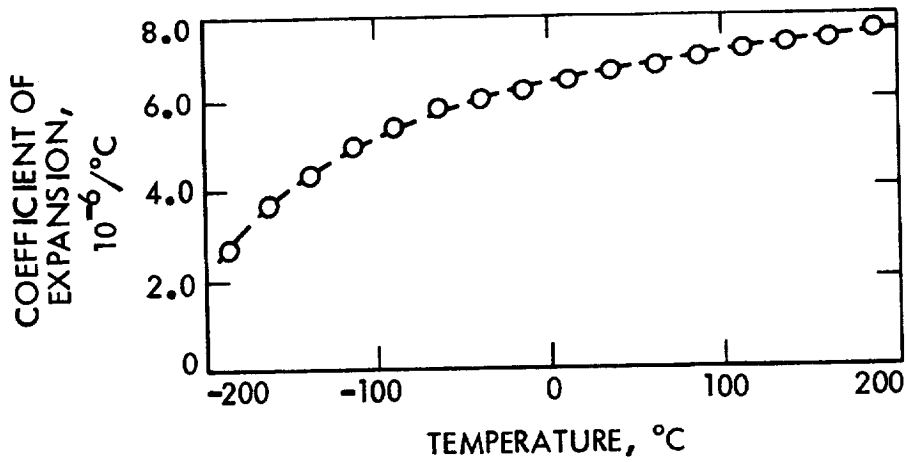
Fig. 7. Instantaneous coefficient of expansion of 0211 glass as a function of temperature
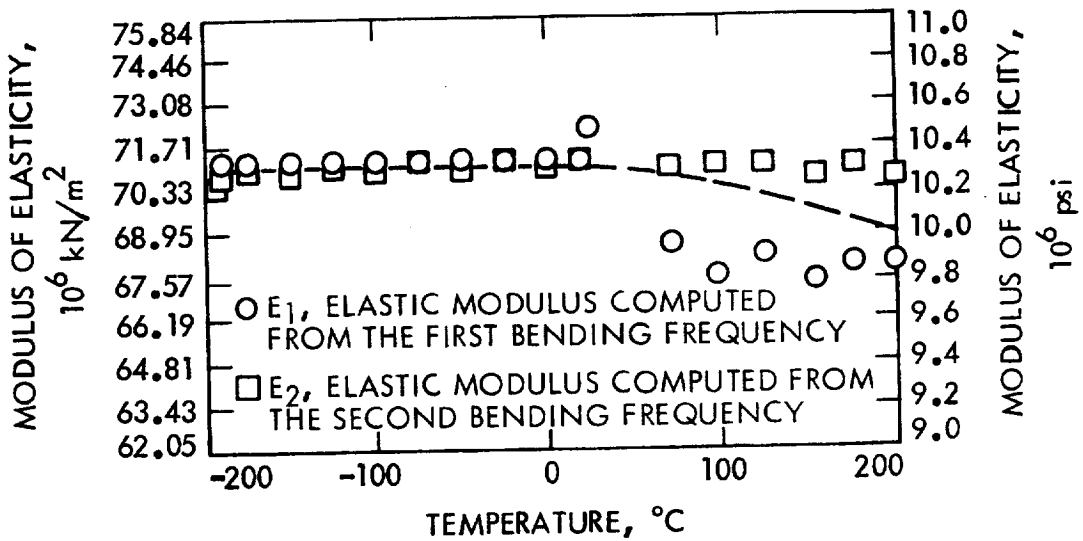
Fig. 8. Modulus of elasticity as a function of temperature for 0211 glass
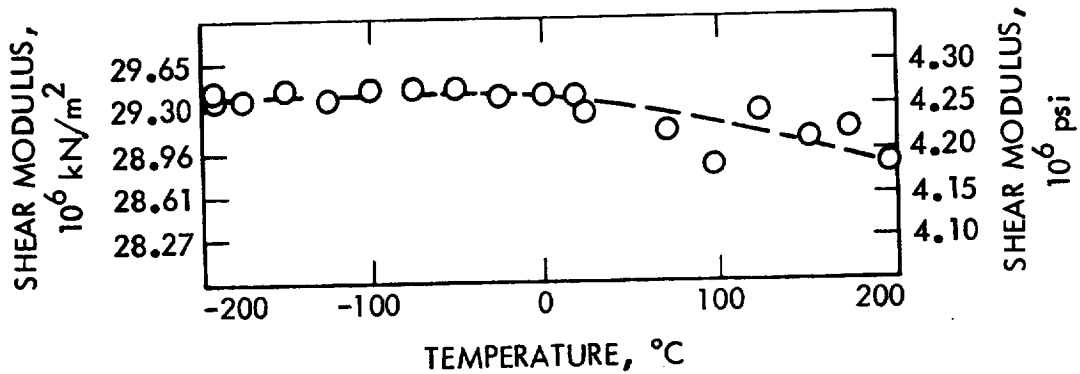
Fig. 9. Shear modulus as a function of temperature for 0211 glass
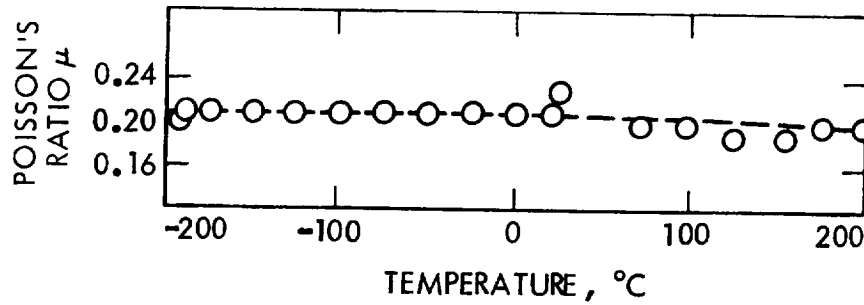
Fig. 10. Poisson's ratio as a function of temperature for 0211 glass
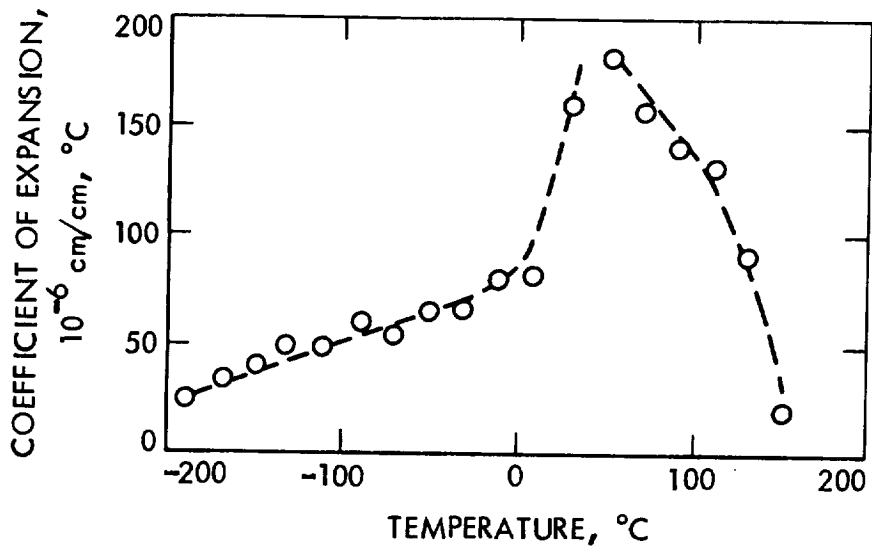
Fig. 11. Instantaneous coefficient of expansion of Tedlar vs temperature
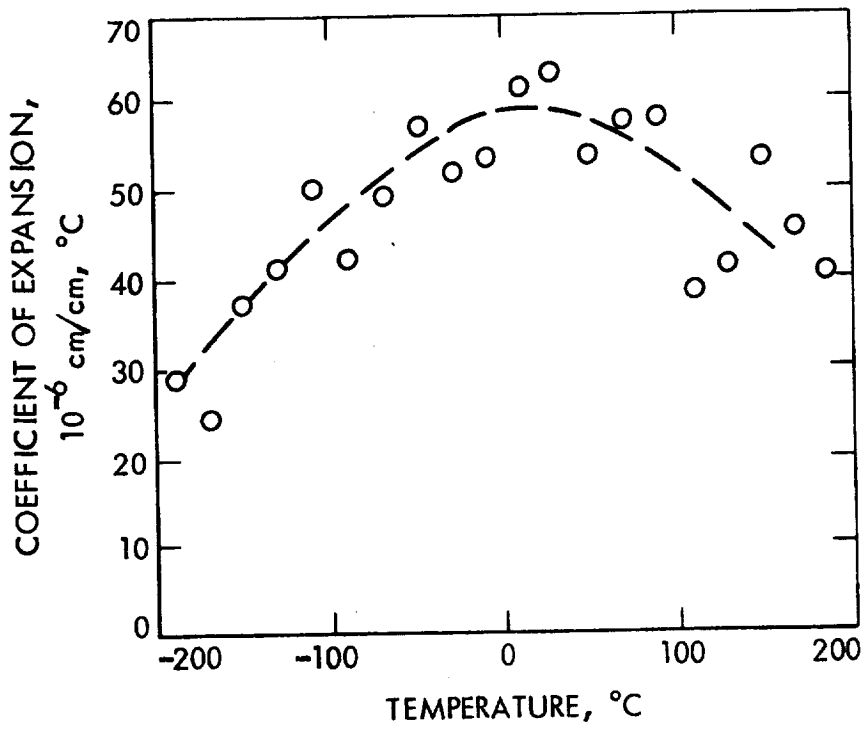
Fig. 12. Instantaneous coefficient of expansion of Kapton-F vs temperature
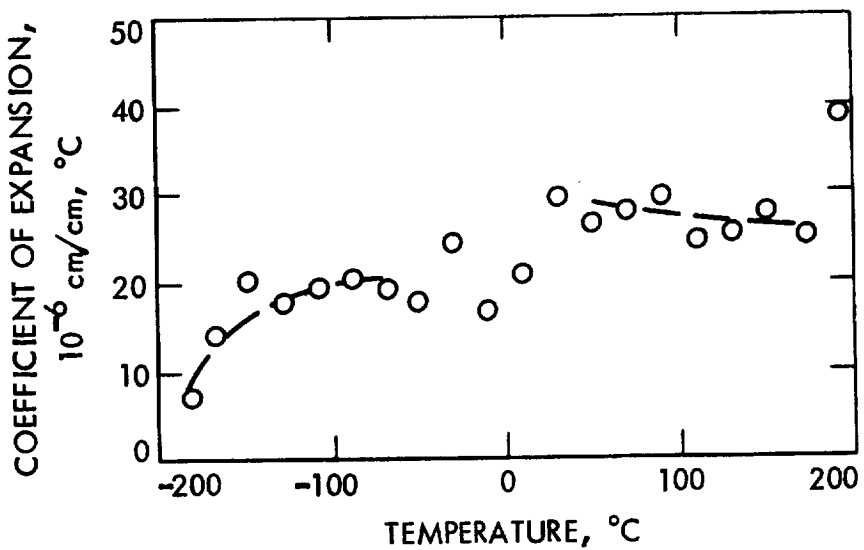
Fig. 13. Instantaneous coefficient of expansion of Kapton-H vs temperature
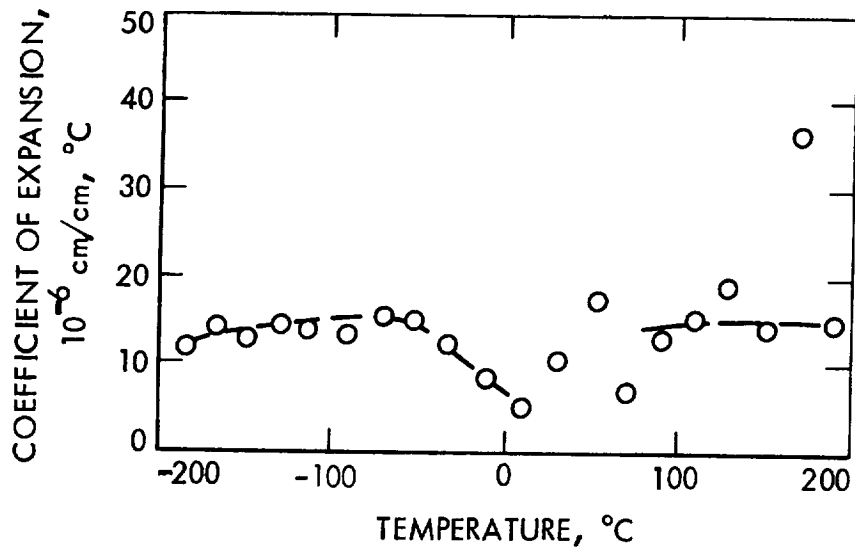
Fig. 14. Instantaneous coefficient of expansion of Mica Ply vs temperature
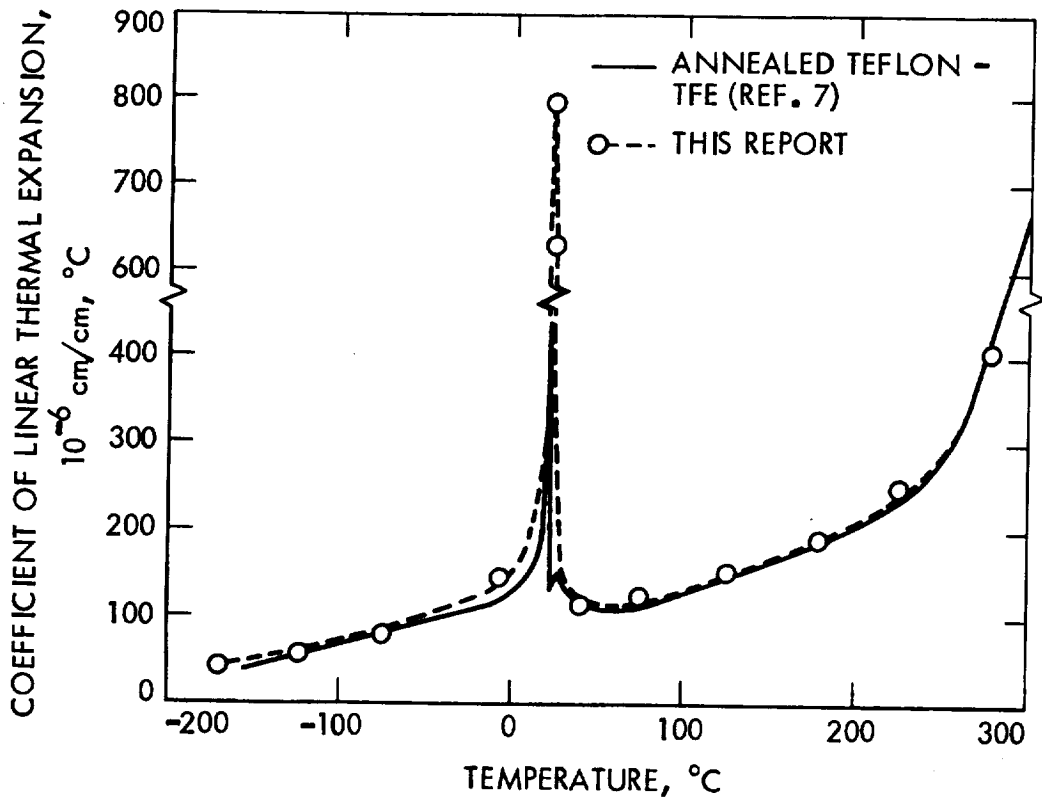
Fig. 15. Instantaneous coefficient of expansion of Teflon vs temperature
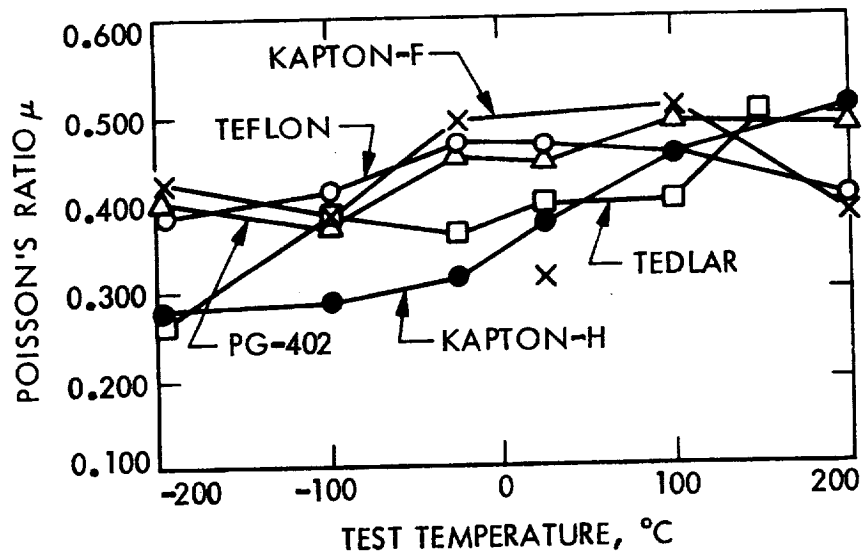
Fig. 16. Poisson's ratio vs temperature for
five materials
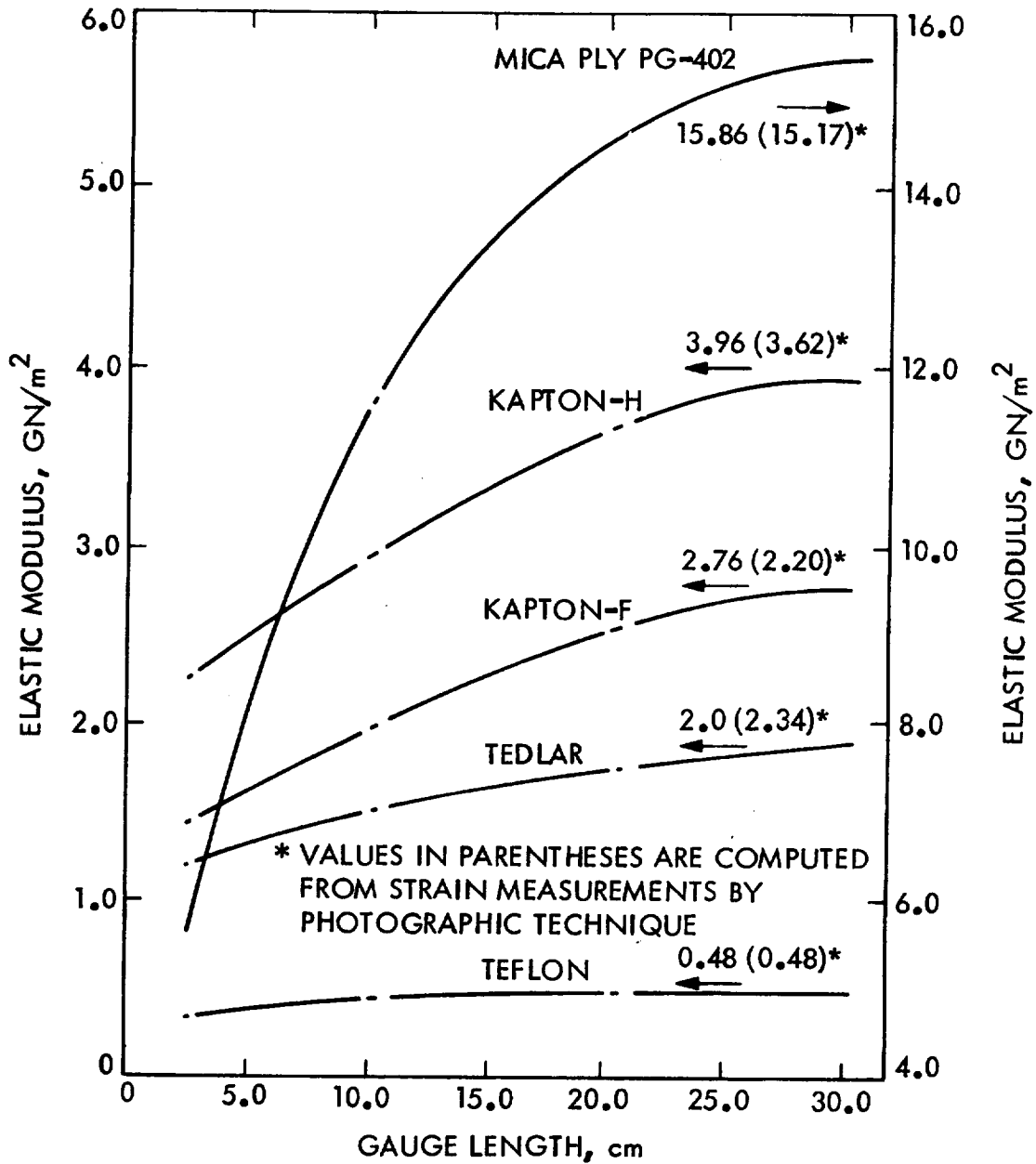
Fig. 17. Elastic modulus variation with gauge length at 25°C: an alternative approach to establish correction factor for gauge length effect on modulus values
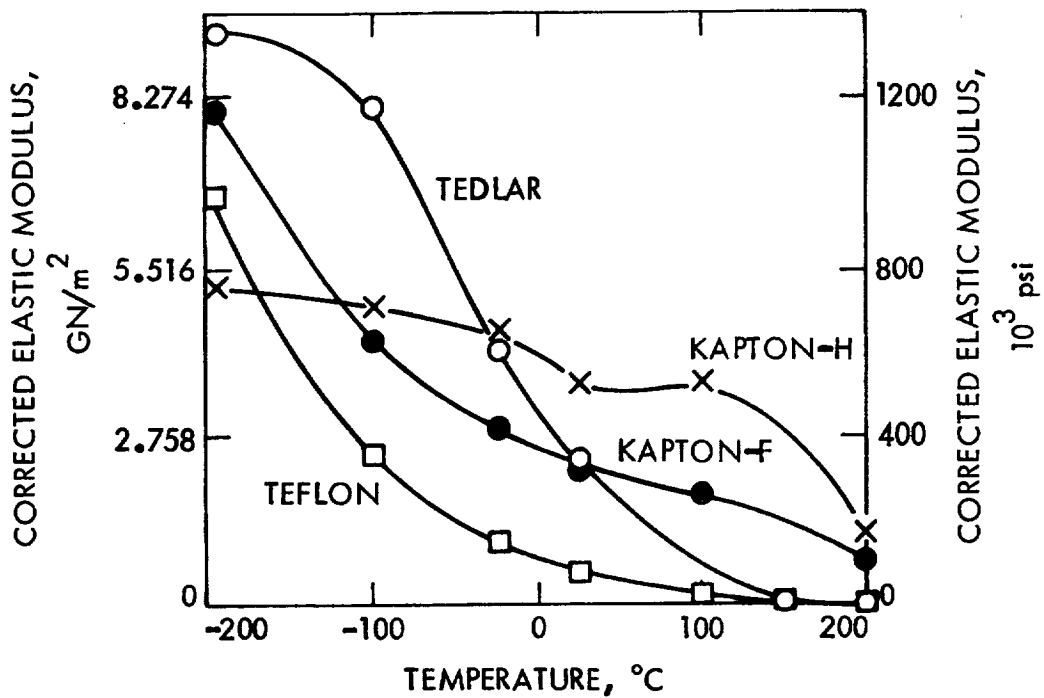
Fig. 18. Corrected elastic modulus vs test temperature for tensile loading (materials as marked)
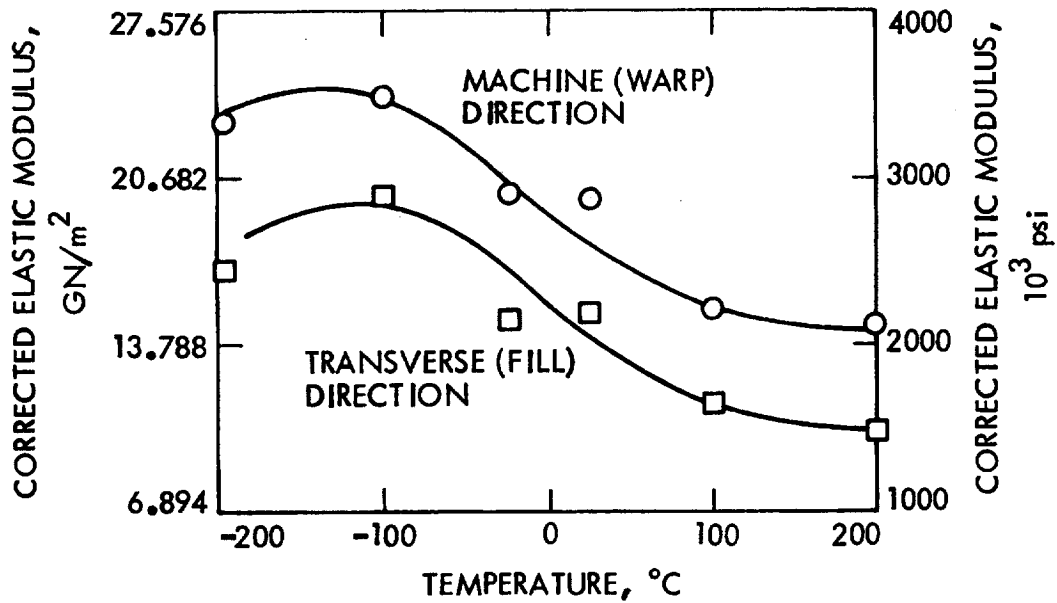
Fig. 19. Corrected elastic modulus vs test temperature for tensile loading of PG-402 fiberglass composite
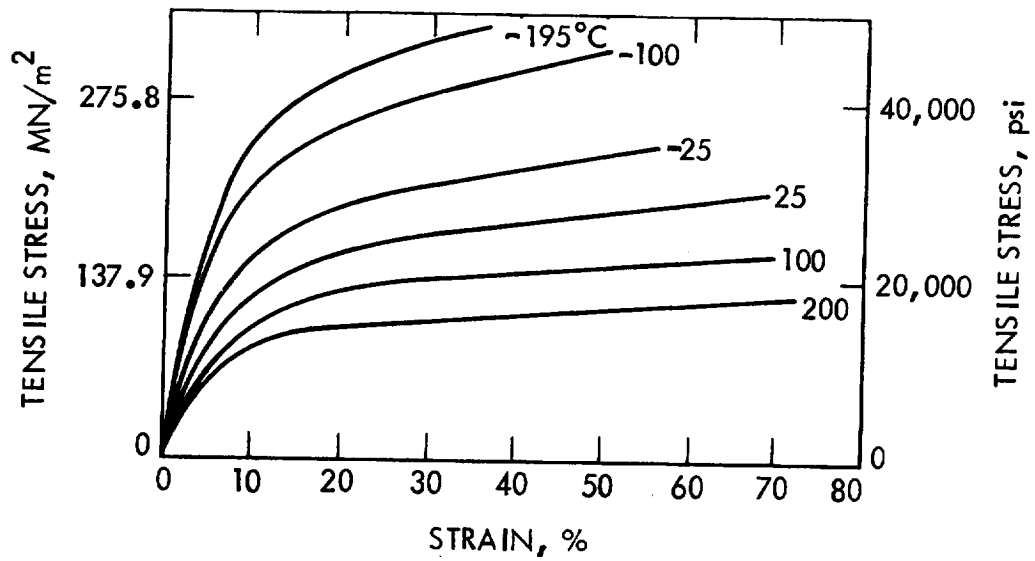
Fig. 20. Typical tensile stress-strain curves for Kapton-H
(0.00762-cm, 0.003-in. thick)
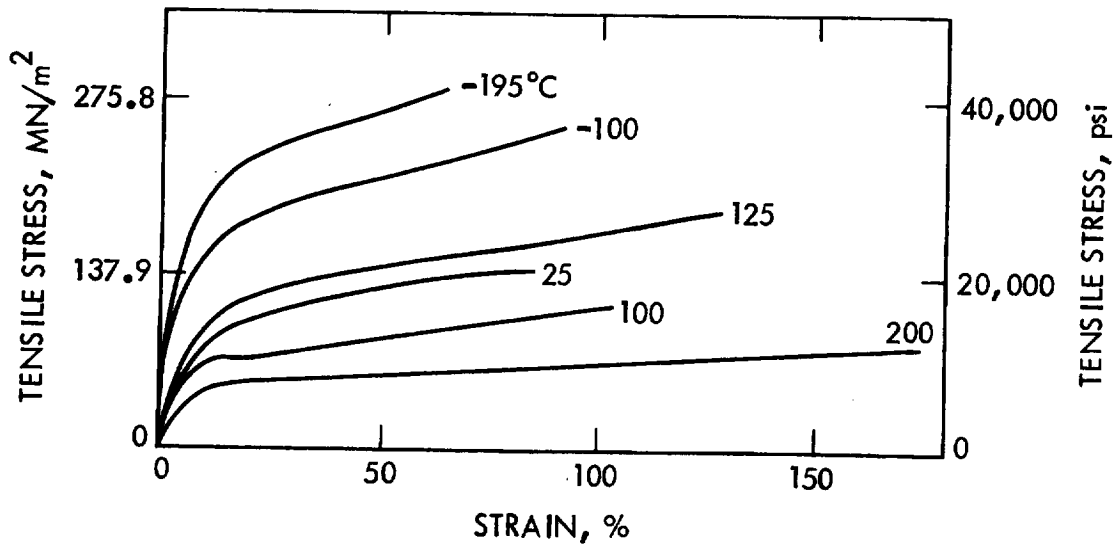
Fig. 21. Typical tensile stress-strain curves for Kapton-F
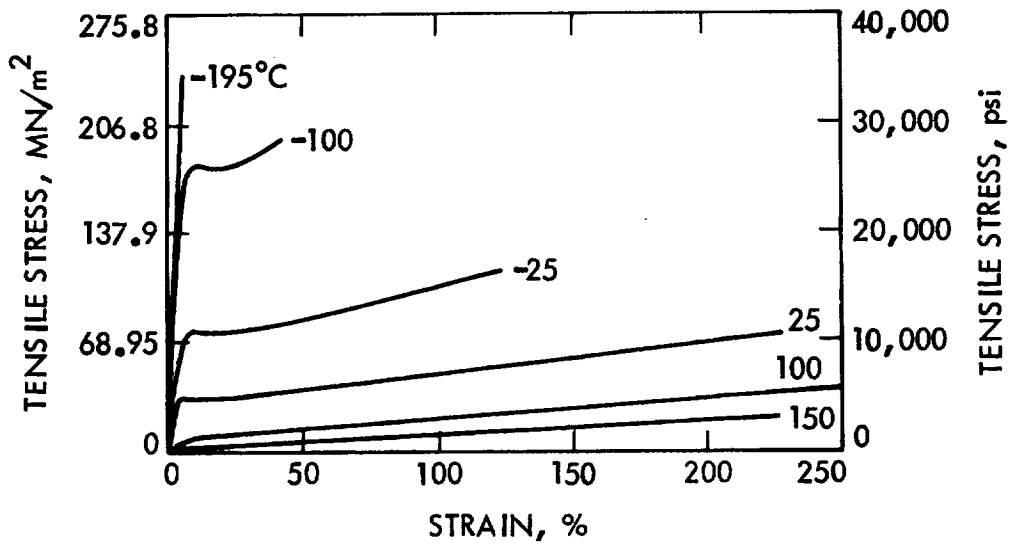(0.00762-cm, 0.003-in. thick)
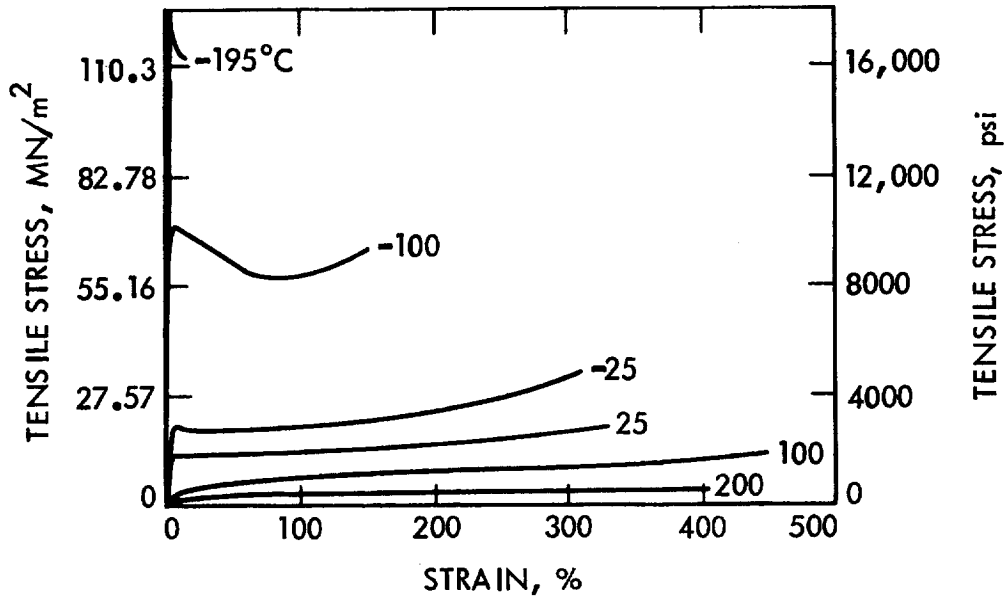
Fig. 22. Typical tensile stress-strain curves for Teflon
(0.00762-cm, 0.003-in. thick)

Fig. 23. Typical tensile stress-strain curves for Tedlar
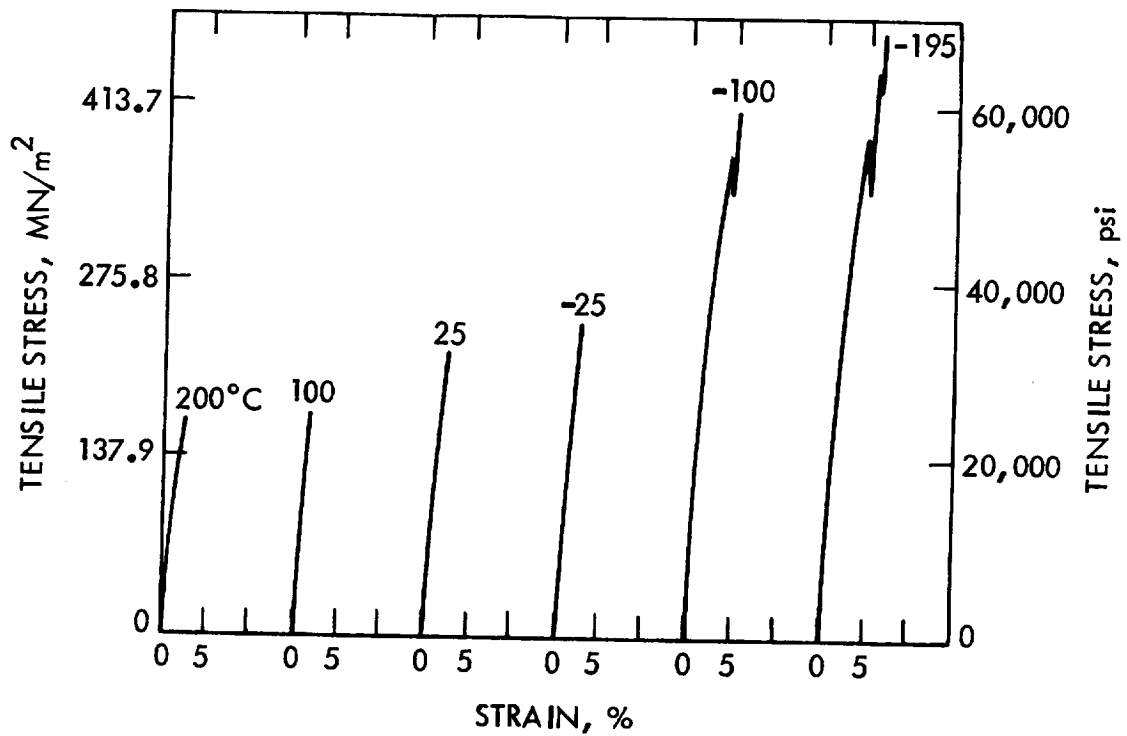(0.0051-cm, 0.002-in. thick)

Fig. 24. Typical tensile stress-strain curves for PG-402
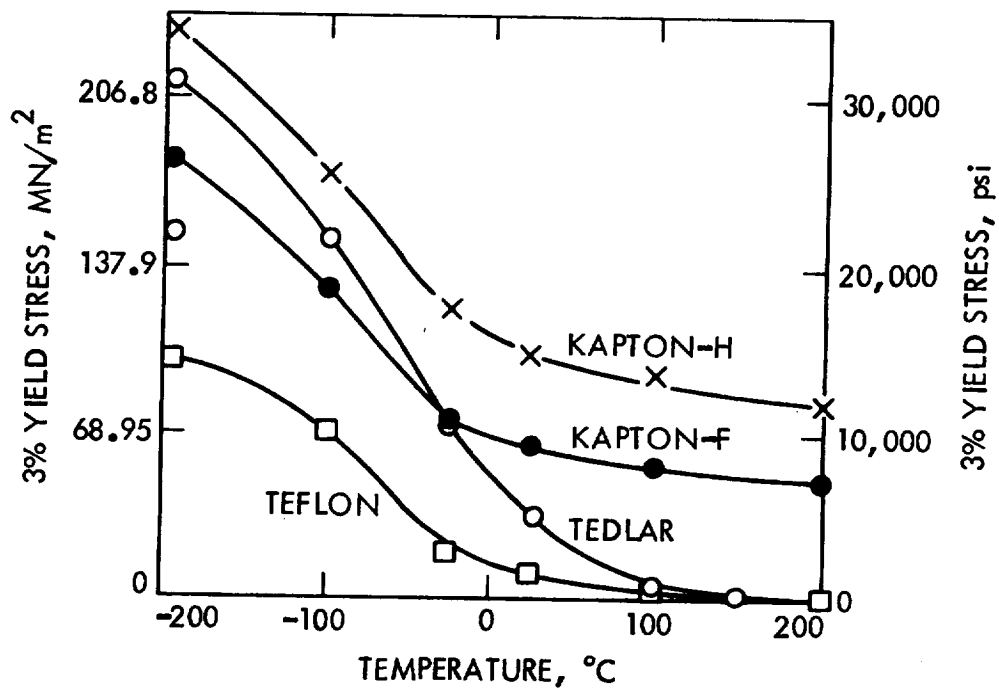fiberglass composite (0.00635-cm, 0.0025-in. thick)

Fig. 25. 3% yield stress vs test temperature for
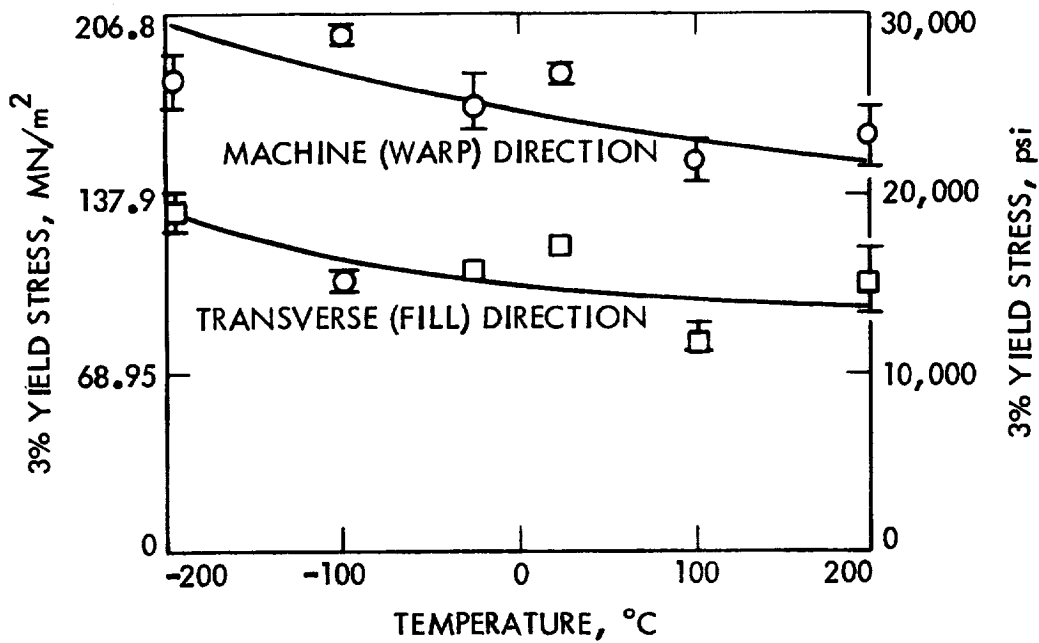tensile loading (materials as marked)

Fig. 26. Yield stress vs test temperature for tensile loading of PG-402 fiberglass composite
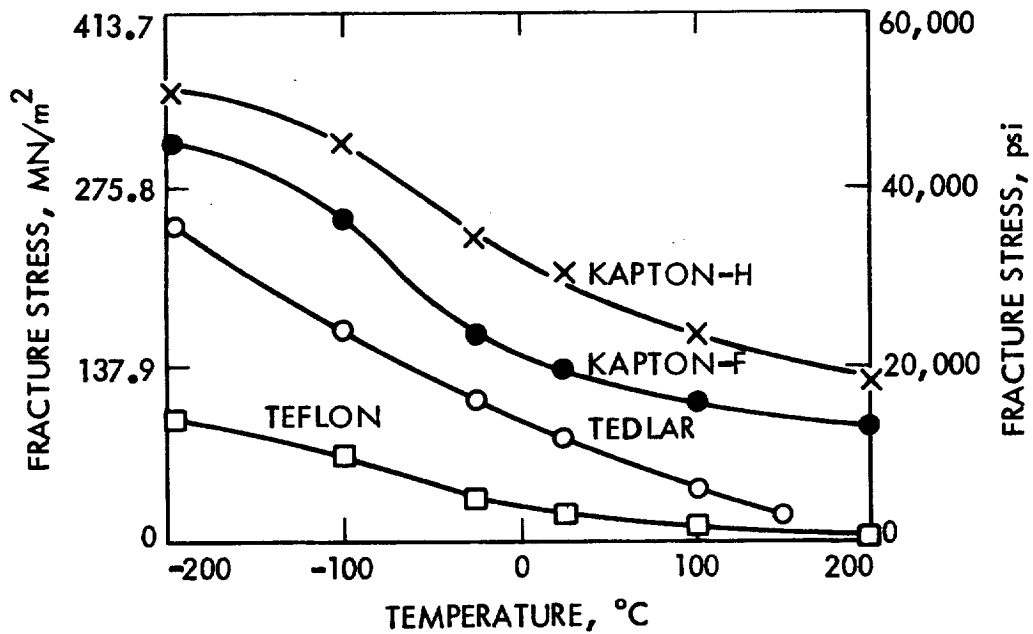

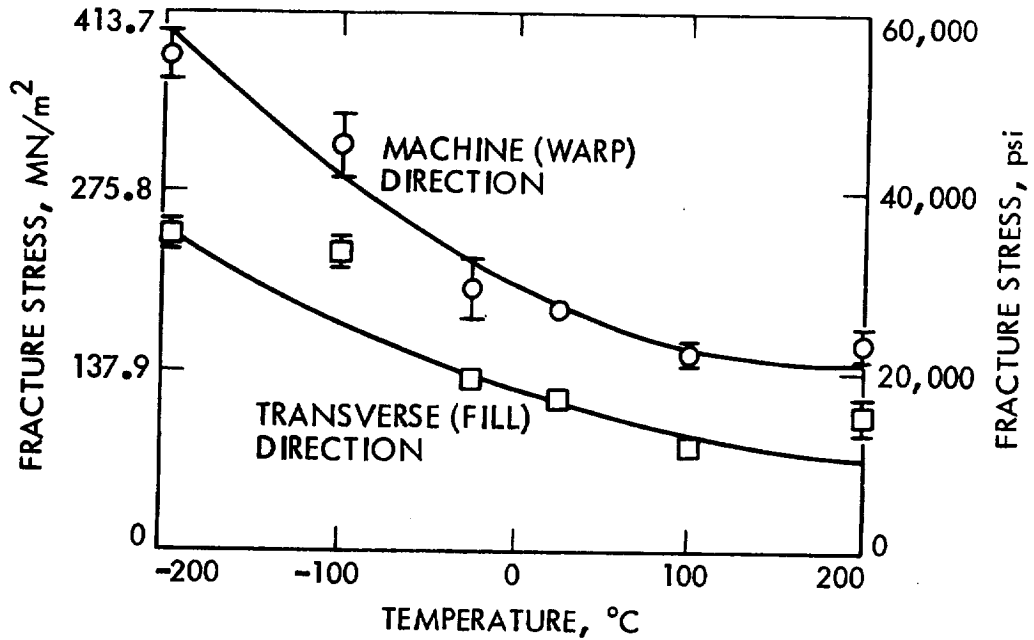Fig. 27. Fracture stress vs test temperature for tensile loading (materials as marked)

Fig. 28. Fracture stress vs test temperature for tensile loading
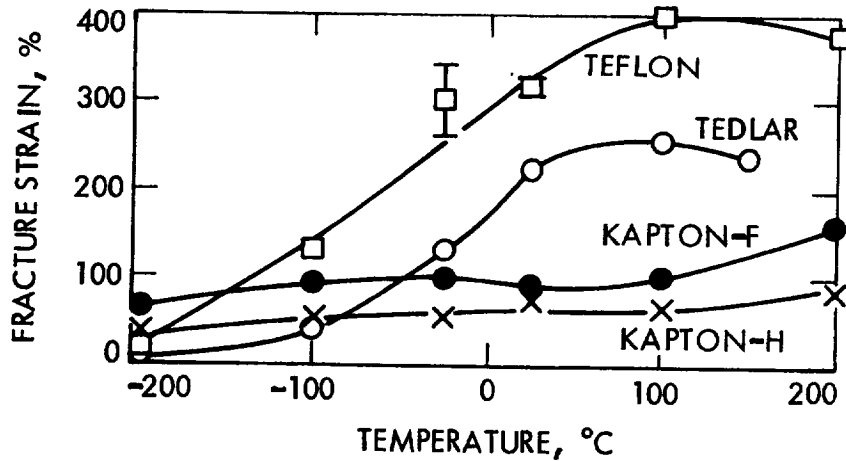of PG-402 fiberglass composite

Fig. 29. Strain to fracture vs test temperature for
tensile loading

APPENDIX A

STRESS COMPUTATION IN DISPLACEMENT METHODS
FOR TWO-MATERIAL ELASTIC MEDIA

I. INTRODUCTION

The stress computation in displacement methods for the structures of two- and three-dimensional continua is an important aspect of a systematic structural analysis. Once the displacements are computed at the nodes of a finite element mesh covering the material volume of the structure, the problem of stress computation at the nodes may be handled in various ways (Refs. 12-19). For example, a usual procedure is to compute stresses from the conditions of compatibility and constitutive relations (Ref. 12). In addition, various schemes of stress averaging (Ref. 13), best fit strains (Ref. 14), and virtual strains (Ref. 15) have been recommended. Stresses obtained by these procedures do not necessarily satisfy the conditions of force equilibrium, especially at boundary points. Recently, an improvement upon these methods has been suggested (Ref.16) in a computational procedure where equilibrium equations are used at the nodes along with the principle of virtual displacements to establish a local stress distribution. No constitutive relationships were used. In this appendix a similar treatment is offered to improve upon the values of internal stresses in continua having more than one material. The work was originally motivated by the fact that when more than one material is involved in the finite element model, and when the stresses are computed on the basis of compatibility and constitutive relations alone, severe violation of force equilibrium may take place at the intermaterial boundary points. Stronger violation of equilibrium conditions is associated with greater differences between the properties of adjacent materials. The approach taken here is concerned with a generalization of the method of best fit strain tensors (Ref. 14) for the stress computation at intermaterial boundary points, so that compatibility, constitutive, and equilibrium conditions are satisfied.

The method of best fit strain tensors was found convenient and economical. It has been in use in several computer codes (Refs. 20-22) for elastic and inelastic materials undergoing geometrically linear deformations. In the following, the method is summarized; then a generalization of the method to handle intermaterial boundary points of two-material continua is presented, and examples of results obtained are given. Again, the objective here is maintaining accuracy while insuring equilibrium, compatibility and the satisfaction of the constitutive relationship. Satisfying the constitutive relationship is especially important when dealing with inelastic material behaviour.

II. THE METHOD OF BEST FIT STRAIN TENSORS

This method of stress computation is modular, not in mesh elements (i.e., finite elements) but in _node sets_. A node set associated with a node is defined (Ref. 14) as the list of nodes coincident with the vertices of all mesh elements meeting at that node. The set of nodal lines joining the node with the other nodes listed in the nodal set is called the _nodal line set_. Numerical

descriptions, in appropriate coordinate systems, are required for the following for all nodes:

(1)   Position vectors.

(2)   Displacement and/or rotation vectors.

(3)   Prescribed forces.

(4)   Reactions, if they exist.

(5)   Material matrices and prescribed initial strains.

(6)   List of boundary point nodes.

(7)   Node sets of the nodes.

Items (1), (3), and (5) are part of the data necessary for the displacement method of analysis. Items (6) and (7) can be easily extracted from the mesh topology information (the list of integers identifying the node labels of the vertices of mesh elements). Item (2) is available as a result of the displacement analysis, and item (4) is usually available as a result of the equilibrium check for the computed deflections. Thus no additional data is required for the method, other than that required by the preceding displacement analysis. Since the stress computation is modular in node sets, the cost of computation varies linearly with the total number of nodes. Moreover, any error committed at a node during the stress computation is confined to that node only. The method is described here for a three-dimensional continuum with no initial stress. For other cases, one may refer to Refs. 14 and 20.

A.   STRESS COMPUTATION AT A NON-BOUNDARY NODE

Let (x_1, x_2, x_3) denote a suitably selected right-hand cartesian coordinate system with its origin located at the node. One may use this coordinate system for the numerical descriptions of position, displacement, and rotation vectors, stress and strain tensors, the material matrix, and the loads. Let $\sigma_{\alpha\beta}$, $\epsilon_{\alpha\beta}$, and u_α, $\alpha = 1,2,3$, and $\beta = 1,2,3$ denote the descriptions of the stress, strain, and displacement at this node. Define $\underline{\Sigma}$, $\underline{E}$, and $\underline{u}$ such that

$$\underline{\Sigma} = \begin{bmatrix} \sigma_{11} & \sigma_{12} & \sigma_{13} \\ & \sigma_{22} & \sigma_{23} \\ \text{Sym} & & \sigma_{33} \end{bmatrix} \tag{A-1}$$

$$\underline{E} = \begin{bmatrix} \epsilon_{11} & \epsilon_{12} & \epsilon_{13} \\ & \epsilon_{22} & \epsilon_{23} \\ \text{Sym} & & \epsilon_{33} \end{bmatrix} \tag{A-2}$$

$$\underline{u}^T = [u_1, u_2, u_3] \qquad\qquad\qquad (A-3)$$

Also, let

$$\underline{\sigma}^T = \left[\sigma_{11}, \ \sigma_{22}, \ \sigma_{12}, \ \sigma_{33}, \ \sigma_{13}, \ \sigma_{23}\right], \qquad (A-4)$$

and

$$\underline{\epsilon}^T = \left[\epsilon_{11}, \ \epsilon_{22}, \ 2\epsilon_{12}, \ \epsilon_{33}, \ 2\epsilon_{13}, \ 2\epsilon_{23}\right]. \qquad (A-5)$$

With the latter notation, the stress-strain relationship may be stated as

$$\underline{\sigma} = \underline{D}\,\underline{\epsilon}. \qquad\qquad\qquad (A-6)$$

where $\underline{D}$ is the material matrix. Note that $\underline{D} = \underline{D}^T$, and $\underline{D}$ is positive definite. Let m denote the total number of nodal lines in the nodal line set of the node. Let ρ^i denote the unit vector in the direction of the ith nodal line. With $\underline{u}^i$ denoted as the relative displacement of the ith node in the node set relative to the node at the origin, and ϵ^i as the lineal strain in the direction of the ith nodal line, we may write

$$\epsilon^i = \underline{\rho}^{i^T} \underline{E}\, \underline{\rho}^i \qquad\qquad\qquad (A-7)$$

where no sum is implied by the repetition of index i. For the strain along the ith nodal line, one may also write

$$\epsilon^i \cong \underline{\rho}^{i^T} \underline{u}^i - \epsilon^i_0 , \qquad\qquad\qquad (A-8)$$

where ϵ_0^i is the prescribed strain in the direction of the ith nodal line. Instead of Eq. (A-8), it is possible to use a higher-order approximation (Ref. 23). However, if the mesh is sufficiently refined, there is no need for such a scheme. By equating the right-hand sides of Eqs. (A-7) and (A-8),

$$\underline{\rho}^{i^T} \underline{E}\, \underline{\rho}^i = \underline{\rho}^{i^T} \underline{u}^i - \epsilon^i_0 , \qquad\qquad\qquad (A-9)$$

or by means of the definitions in Eqs. (A-2) and (A-5),

$$\underline{r}_i^T \, \underline{\epsilon} = \underline{\rho}^i \, \underline{u}^i - \epsilon_0^i, \qquad i = 1, \dots, m, \qquad \text{(A-10)}$$

where

$$\underline{r}_i^T = \left[\rho_1^i \rho_1^i, \ \rho_2^i \rho_2^i, \ \rho_1^i \rho_2^i, \ \rho_3^i \rho_3^i, \ \rho_1^i \rho_3^i, \ \rho_2^i \rho_3^i \right]. \qquad \text{(A-11)}$$

Let

$$\underline{R} = \left[\underline{r}_1, \ \underline{r}_2, \ \dots, \ \underline{r}_m \right], \qquad \text{(A-12)}$$

and

$$\underline{\epsilon}^{0^T} = \left[\left(\underline{\rho}^{1^T} \underline{u}^1 - \epsilon_0^1 \right), \ \left(\underline{\rho}^{2^T} \underline{u}^2 - \epsilon_0^2 \right), \ \dots, \ \left(\underline{\rho}^{m^T} \underline{u}^m - \epsilon_o^m \right) \right]. \qquad \text{(A-13)}$$

Then, Eq. (A-10) may be rewritten as

$$\underline{R}^T \, \underline{\epsilon} = \underline{\epsilon}^0 \qquad \text{(A-14)}$$

For most finite element meshes, $m \geq 6$. One can always choose a finite element mesh such that $m \geq 6$. From Eq. (A-14), $\underline{\epsilon}$ can be determined by the least squares as

$$\underline{\epsilon} = \left(\underline{R} \, \underline{R}^T \right)^{-1} \underline{R} \, \underline{\epsilon}^0. \qquad \text{(A-15)}$$

The substitution of $\underline{\epsilon}$ from Eq. (A-15) into Eq. (A-6) yields

$$\underline{\sigma} = \underline{D} \left(\underline{R} \, \underline{R}^T \right)^{-1} \underline{R} \, \underline{\epsilon}^0 \qquad \text{(A-16)}$$

which is a good approximation of the stresses at the node.

B.   STRESS COMPUTATION AT A BOUNDARY NODE

Here we have the additional constraint that the internal stresses should be in equilibrium with the boundary tractions. Let $\underline{p}$ denote the known boundary force vector at the node. From the mesh data, it is possible to compute an average boundary surface area A such that the boundary tractions $\underline{\sigma}_0$ at the node may be approximated as

$$\underline{\sigma}_0 = \frac{1}{A} \underline{p} \cdot \qquad \text{(A-17)}$$

Using the mesh data it is also possible to compute the description of the unit outer normal n of the boundary surface at the node. The equilibrium equations at the node may be written as

$$\underline{\Sigma} \underline{n} = \underline{\sigma}_0 , \qquad \text{(A-18)}$$

Or using the definition in Eq. (A-4),

$$\underline{B} \underline{\sigma} = \underline{\sigma}_0 , \qquad \text{(A-19)}$$

where

$$\underline{B} = \begin{bmatrix} n_1 & \cdot & n_2 & \cdot & n_3 & \cdot \\ \cdot & n_2 & n_1 & \cdot & \cdot & n_3 \\ \cdot & \cdot & \cdot & n_3 & n_1 & n_2 \end{bmatrix} \cdot \qquad \text{(A-20)}$$

Substitution of $\underline{\sigma}$ from Eq. (A-6) into Eq. (A-19) yields

$$\underline{B} \underline{D} \underline{\epsilon} = \epsilon_0 ; \qquad \text{(A-21)}$$

Scaling both sides of this equation with (1,1) element of $\underline{D}$, $d_{1,1}$ gives

$$\underline{S} \underline{\epsilon} = \underline{\epsilon}_0 , \qquad \text{(A-22)}$$

where

$$\underline{S} = \frac{1}{d_{1,1}} \underline{B} \underline{D} , \qquad \text{(A-23)}$$

and

$$\underline{\epsilon}_0 = \frac{1}{d_{1,1}} \underline{\sigma}_0 \quad . \tag{A-24}$$

The strain-deflection equations of the nodal line set are as in Eq. (A-14). Combining Eqs. (A-14) and (A-22),

$$\begin{bmatrix} \underline{R}^T \\ \text{---} \\ \underline{S} \end{bmatrix} \epsilon = \left\{ \begin{array}{c} \underline{\epsilon}^0 \\ \text{---} \\ \underline{\epsilon}_0 \end{array} \right\} \quad , \tag{A-25}$$

where $\underline{\epsilon}$ may be solved by least squares as

$$\underline{\epsilon} = \left(\underline{R}\,\underline{R}^T + \underline{S}^T\underline{S} \right)^{-1} \left(\underline{R}\,\underline{\epsilon}^0 + \underline{S}^T\underline{\epsilon}_0 \right) \tag{A-26}$$

The substitution of $\underline{\epsilon}$ from Eq. (A-26) into Eq. (A-6) yields the desired stresses.

Alternatively, from Eq. (A-22), one can solve for some of the components of $\underline{\epsilon}$ in terms of the remaining components. Let $\underline{\epsilon}'$ and $\underline{\epsilon}''$, respectively, denote the independent and the dependent components of $\underline{\epsilon}$. The choice of $\underline{\epsilon}'$ can be made such that

$$\underline{\epsilon}^T = \left[\underline{\epsilon}'^T , \ \underline{\epsilon}''^T \right] \quad . \tag{A-27}$$

Calling the corresponding conformable partitions of $\underline{S}$, $\underline{S}'$ and $\underline{S}''$, one obtains

$$\underline{S} = [\underline{S}' , \underline{S}''] \quad . \tag{A-28}$$

Rewriting Eq. (A-22) with the definitions in Eqs. (A-27) and (A-28) yields

$$\underline{S}'\,\underline{\epsilon}' + \underline{S}''\,\underline{\epsilon}'' = \underline{\epsilon}_0 \quad . \tag{A-29}$$

From this equation, $\underline{\epsilon}''$ may be solved as

$$\underline{\epsilon}'' = -\underline{S}''^{-1}\,\underline{\epsilon}' + \underline{S}''^{-1}\underline{\epsilon}_0 \quad . \tag{A-30}$$

Combining this equation with the identity

$$\underline{\epsilon}' = \underline{I}\,\underline{\epsilon}' + 0\,\underline{\epsilon}_0 \quad , \tag{A-31}$$

one may express Eq. (A-22) as

$$\underline{\epsilon} = \begin{bmatrix} \underline{I} \\ ----- \\ -\underline{S}''^{-1} \end{bmatrix} \epsilon' + \begin{bmatrix} \underline{0} \\ ---- \\ \underline{S}''^{-1} \end{bmatrix} \underline{\epsilon}_0 \quad . \tag{A-32}$$

Defining

$$\underline{G} = \begin{bmatrix} \underline{I} \\ ---- \\ -\underline{S}''^{-1} \end{bmatrix} \quad , \tag{A-33}$$

and

$$\underline{H} = \begin{bmatrix} \underline{0} \\ ---- \\ \underline{S}''^{-1} \end{bmatrix} \quad , \tag{A-34}$$

one may write Eq. (A-32) as

$$\underline{\epsilon} = \underline{G}\,\epsilon' + \underline{H}\,\underline{\epsilon}_0 \quad . \tag{A-35}$$

Now, substituting $\underline{\epsilon}$ from Eq. (A-35) into Eq. (A-14) yields

$$\underline{R}^T\,\underline{G}\,\underline{\epsilon}' = \underline{\epsilon}^0 - \underline{R}^T\,\underline{H}\,\underline{\epsilon}_0 \quad . \tag{A-36}$$

By applying the least squares scheme, from Eq. (A-36), one may express $\underline{\epsilon}'$ as

$$\underline{\epsilon}' = (\underline{G}^T\underline{R}\,\underline{R}^T\underline{G})^{-1}(\underline{G}^T\underline{R}\,\underline{\epsilon}^0 - \underline{G}^T\underline{R}\underline{R}^T\,\underline{H}\,\underline{\epsilon}_0) \tag{A-37}$$

The substitution of $\underline{\epsilon}'$ from Eq. (A-37) into Eq. (A-35) yields the strains $\underline{\epsilon}$, and then Eq. (A-6) may be used to compute the stresses. In this alternate way, the stress equilibrium equations of Eq. (A-19) are satisfied without error.

III. THE METHOD OF BEST FIT STRAIN TENSORS FOR TWO-MATERIAL NODES

The method of best fit strain tensors may be used for the computation of stresses at the nodes involving two different materials as described below. To simplify the presentation, it will be assumed that the node is not on the overall boundary of the structure, and that the structure is a three-dimensional continuum. The procedure requires the identification of all two-material nodes. For this, the usual input data of displacement analysis is sufficient. In order to simplify the computations, the local coordinate system (x_1, x_2, x_3) is oriented such that the x_2-axis is normal to the intermaterial boundary at the node. The development presented in the following paragraphs may be used directly for the two-dimensional continua if the x_3-axis is oriented in the thickness direction.

In addition to the satisfaction of both the stress-strain and the strain-deflection relations, the stress computation at a two-material point also requires that (1) the strains at both sides of the intermaterial boundary maintain the <u>no-slip</u> condition, and (2) the stresses at both sides of the intermaterial boundary satisfy the <u>equilibrium</u> conditions.

Let the superscripts 1 and 2 denote the first and second material, respectively. With this, the stress-strain relations may be written as

$$\underline{\sigma}^j = \underline{D}^j \underline{\epsilon}^j \quad , \quad j = 1, 2 \tag{A-38}$$

where it is assumed that both of the material matrices are known.

A. NO-SLIP CONDITIONS ON INTERMATERIAL BOUNDARY

These conditions may be expressed by

$$\epsilon_{11}^1 + \tilde{\epsilon}_{011}^1 = \epsilon_{11}^2 + \tilde{\epsilon}_{011}^2 \quad ,$$

$$\epsilon_{33}^1 + \tilde{\epsilon}_{033}^1 = \epsilon_{33}^2 + \tilde{\epsilon}_{033}^2 \quad , \tag{A-39}$$

$$\epsilon_{13}^1 + \tilde{\epsilon}_{013}^1 = \epsilon_{13}^2 + \tilde{\epsilon}_{013}^2 \quad ,$$

and where $\tilde{\epsilon}_{011}^i$, $\tilde{\epsilon}_{033}^i$, and $\tilde{\epsilon}_{013}^i$, $i = 1, 2$ are the prescribed strains.

Equation (A-39) may be rewritten as

$$\underline{N}\,(\underline{\varepsilon}^1 + \underline{\tilde{\varepsilon}}_0^{\,1}) = \underline{N}\,(\underline{\varepsilon}^2 + \underline{\tilde{\varepsilon}}_0^{\,2}) \qquad \qquad \text{(A-40)}$$

where

$$N = \begin{bmatrix} 1 & . & . & . & . & . \\ . & . & . & 1 & . & . \\ . & . & . & . & 1 & . \end{bmatrix} \qquad \text{(A-41)}$$

and $\underline{\tilde{\varepsilon}}_0^{\,1}$, $i = 1,2$, are the vectors listing the prescribed strains of the two materials. Note that the no-slip conditions state the uniqueness of the strain components on the plane of the intermaterial boundary at the node.

B. EQUILIBRIUM OF STRESSES ACTING ON INTERMATERIAL BOUNDARY

The equilibrium of stresses acting on the intermaterial boundary may be expressed as

$$\sigma^1_{22} = \sigma^2_{22} \quad , \quad \sigma^1_{12} = \sigma^2_{12} \quad , \quad \text{and} \quad \sigma^1_{23} = \sigma^2_{23} \quad . \quad \text{(A-42)}$$

These may be rewritten as

$$\underline{M}\,\underline{D}^1\,\underline{\varepsilon}^1 = \underline{M}\,\underline{D}^2\,\underline{\varepsilon}^2 \quad , \qquad \qquad \text{(A-43)}$$

where

$$\underline{M} = \frac{1}{d^1_{1,1}} \begin{bmatrix} . & 1 & . & . & . & . \\ . & . & 1 & . & . & . \\ . & . & . & . & . & 1 \end{bmatrix} \quad . \qquad \text{(A-44)}$$

Note that $d_1^{\,1}{}_{,1}$ is the (1,1) element of $\underline{D}^1$.

C. COMBINED NO-SLIP/EQUILIBRIUM CONDITIONS

Equations (A-40) and (A-44) may be combined in the following form

$$\underline{C}^1 \underline{\epsilon}^1 + \underline{b} = \underline{C}^2 \underline{\epsilon}^2 \quad , \tag{A-45}$$

where

$$\underline{C}^j = \begin{bmatrix} \underline{M} \underline{D}^j \\ ---- \\ \underline{N} \end{bmatrix} \quad , \quad j=1,2 \quad . \tag{A-46a}$$

and

$$\underline{b}^T = \left[0, 0, 0, (\tilde{\epsilon}^1_{011} - \tilde{\epsilon}^2_{011}), (\tilde{\epsilon}^1_{033} - \tilde{\epsilon}^2_{033}), (\tilde{\epsilon}^1_{013} - \tilde{\epsilon}^2_{013}) \right] \quad . \tag{A-46b}$$

It can be shown that $\underline{C}^j$, j=1,2, are not singular, so long as $\underline{D}^j$, j=1,2, are positive definite.

D. STRAIN-DEFLECTION RELATIONS

The intermaterial boundary divides the nodal line set of the node into two partitions. The nodal lines of the intermaterial boundary may be included in both partitions. Let m_j, j=1,2, denote the number of nodal lines in the jth partition. The strain-deflection relations of each partition may be written, similar to Eq. (A-14), as

$$\underline{R}^{j^T} \underline{\epsilon}^j = \underline{\epsilon}^{0j} \quad , \quad j=1,2 \quad , \tag{A-47}$$

where

$$\underline{R}^j = \left[\underline{r}_1, \ldots, \underline{r}_{mj} \right]^j \quad , \quad j=1,2 \quad , \tag{A-48}$$

$$\underline{r}_i^{j^T} = \left[\rho_1^i \rho_1^i, \ \rho_2^i \rho_2^i, \ \rho_1^i \rho_2^i, \ \rho_3^i \rho_3^i, \ \rho_1^i \rho_3^i, \ \rho_2^i \rho_3^i \right]^j, \quad j=1,2 \quad , \tag{A-49}$$

and

$$\underline{\epsilon}^{0j^T} = \left[\left(\underline{\rho}^{1^T} \underline{u}^1 - \epsilon_0^1 \right), \ \ldots, \ \left(\underline{\rho}^{mj^T} \underline{u}^{mj} - \epsilon_0^{mj} \right) \right] \quad , \quad j=1,2 \quad . \tag{A-50}$$

E. COMPUTATION OF STRESSES

Since $\underline{c}^{2-1}$ exists, one may solve $\underline{\epsilon}^2$ from Eq. (A-45) as

$$\underline{\epsilon}^2 = \underline{c}^{2^{-1}} \underline{c}^1 \underline{\epsilon}^1 + \underline{c}^{2^{-1}} \underline{b} \quad . \tag{A-51}$$

Substituting $\underline{\epsilon}^2$ from Eq. (A-51) into Eqs. (A-47), yields

$$\begin{bmatrix} \underline{R}^{1^T} \\ \text{-------} \\ \underline{R}^{2^T} \underline{c}^{2^{-1}} \underline{c}^1 \end{bmatrix} \epsilon^1 = \begin{Bmatrix} \underline{\epsilon}^{01} \\ \text{- - -} \\ \underline{\epsilon}_{*}^{02} \end{Bmatrix} \tag{A-52a}$$

where

$$\underline{\epsilon}_{*}^{02} = \underline{\epsilon}_0^2 - \underline{R}^{2^T} \underline{c}^{2^{-1}} \underline{b} \quad . \tag{A-52b}$$

Equation (A-52a) may be solved for $\underline{\epsilon}^1$ by least squares as

$$\underline{\epsilon}^1 = (\underline{R}^1 \underline{R}^{1^T} + \underline{c}^{1^T} \underline{c}^{2^{-T}} \underline{R}^2 \underline{R}^{2^T} \underline{c}^{2^{-1}} \underline{c}^1)^{-1} (\underline{R}^1 \underline{\epsilon}^{01}$$

$$+ \underline{c}^{1^T} \underline{c}^{2^{-T}} \underline{R}^2 \underline{\epsilon}_{*}^{02}) \quad . \tag{A-53}$$

Once the numerical values of $\underline{\epsilon}^1$ are computed, Eq. (A-51) is used to obtain those of $\underline{\epsilon}^2$. Then using Eq. (A-38), one can obtain the stresses.

IV. EXAMPLES

The following two examples illustrate the numerical results of the computational procedure developed in the previous section. The simple plane stress element with linear displacement field and two degrees of freedom at each node (Ref. 20) was employed.

The first example is that of a force acting at the end of a cantilevered wedge as shown in Fig. A-1. The theory of elasticity solution is given in Ref. 24[4] and is presented at section A-A by the curves labeled "a" in Figs. A-2 and

---

[4]The solution derived in Ref. 24 is for one material only and ignores the clamped boundary conditions.

A-3 for the normal and shear stresses σ_{22} and σ_{12}, respectively. When one uses the finite element model of Fig. A-1, in which the material in region I is different from that in region II ($E_I = 3.0 \times 10^6$, $E_{II} = 1.0 \times 10^6$, $\mu_I = \mu_{II} = 0.3$), the conventional best fit strain method of Section II gives two sets of stresses, one at each side of the intermaterial boundary A-A. These are labeled "b_I" and "b_{II}" in Figs. A-2 and A-3, for material I and material II. Clearly, the two sets of stresses at the intermaterial boundary are not in equilibrium with each other.

Next, the application of the computational procedure developed in Section III with the same finite element model of Fig. A-1 results in two sets of self-equilibrating stresses at the intermaterial boundary. These are coincident and are represented by the curves labeled "c" in Figs. A-2 and A-3. In addition to being in equilibrium, the stresses computed in this manner are more accurate than either "b_I" or "b_{II}". It should be noted, however, that the degree of accuracy is still dependent upon other factors such as the finite element mesh size and the assumed displacement field within the elements; this is treated further in the next example.

In the second example, the stresses produced by cooling an outside cylinder onto an inside one are computed. Initially, the outside radius of the inner cylinder is equal to the inside radius of the outer cylinder (Fig. A-4). Thus, by uniformly cooling the outer cylinder by $T = -200°F$, the stress distribution in the two cylinders can be obtained by the elasticity theory and by the procedures described. Because of the rotational symmetry, it is sufficient to consider only a narrow wedge of the cylinders as shown by the plane-stress finite element model of Fig. A-5a.

Let M1 and M2 be the number of equally spaced intervals in the inner cylinder (material I) and outer cylinder (material II), respectively. Figure A-5b shows the radial stress distribution σ_r^I and σ_r^{II} obtained by the conventional best fit strain method of Section A-II when M1 = M2 = 5. The discontinuity in the radial stresses at the intermaterial boundary indicates the degree of equilibrium violation.

In Table A-1, the intermaterial boundary stress values σ_r^I, σ_r^{II}, and σ_t^I, σ_t^{II} in the radial and tangential directions are given. First, column A gives the theoretical values, against which the finite element solutions in B, C, and D of Table A-1 are compared by forming the percent error (in parenthesis). Next, in group B, Table A-1, the intermaterial boundary stresses of Fig. A-5b for M1 = M2 = 5 are listed for the conventional best fit strain method and followed by the values obtained when equilibrium is enforced according to Section III. The error associated with the conventional best fit strain method with M1 = M2 = 5 varies from +1.17 to +9.84% for σ_r^I, σ_r^{II}, and from +0.7 to -3.3% for σ_t^I, σ_t^{II}. Although the generalized best fit strain method of Section III did not greatly improve upon the errors in this case (+7.3 percent for σ_r^I, σ_r^{II}, and -7.1%, -1.3% for σ_t^I, σ_t^{II}), it has the advantage of producing a more consistent set of stresses which satisfy equilibrium, compatibility and constitutive relations.

The results in group C and D of Table A-1 show that the rate of convergence of stresses as a result of varying the finite element mesh size is almost the same for both computational procedures. Figure A-6, in which the

radial stresses $\sigma_r^{\ I}$, $\sigma_r^{\ II}$ are plotted for different finite element mesh sizes, emphasizes the same conclusion.

V. CONCLUSIONS

Various schemes for the stress computation in the finite element method have been suggested in which either equilibrium of forces or constitutive relations were not necessarily satisfied. Among these schemes is the conventional best fit strain method in which equilibrium is usually not satisfied at the intermaterial boundaries. A generalization of this method was given in Section III, where full account is taken of all conditions of equilibrium, constitutive and compatibility relations. The computation to accomplish this does not require any additional data over that needed for the conventional best fit strain method. Both methods proceed from the basic data necessary for the displacement method of analysis.

From the presented examples it is shown that while the degree of equilibrium violation in the conventional best fit strain method is dependent upon the finite mesh size, overall better accuracy in satisfying equilibrium, constitutive and compatibility relations is achieved in the stresses computed by the generalized best fit strains developed in Section III. Similar improvements can be expected from an analogous generalization of other schemes for the stress computation.

Table A-1. Comparison of intermaterial boundary stresses for two-cylinder shrink fit

Stress component at the boundary	A Theory	B; M1 = M2 = 5		C; M1 = M2 = 10		D; M1 = M2 = 15	
		Conventional best fit strain, Section II	Generalized best fit strain, Section III	Conventional best fit strain, Section II	Generalized best fit strain, Section III	Conventional best fit strain, Section II	Generalized best fit strain, Section III
σ_r^I	-5958	-5888 (+0.0117)	5523 (+0.073)	-5934 (+0.004)	-5738 (+0.037)	-5943 (+0.0025)	-5847 (+0.018)
σ_r^{II}	-5958	-5372 (+0.0984)	-5523	-5678 (+0.047)	-5738	-5821 (+0.0230)	-5847
σ_t^I	-7847	-7395 (+0.007)	-7979 (-0.071)	-7448 (-0.0001)	-7730 (-0.038)	-7449 (-0.0002)	-7589 (-0.019)
σ_t^{II}	+15490	+14985 (-0.033)	+15283 (-0.013)	+15227 (-0.017)	+15379 (-0.007)	+15357 (-0.009)	+15434 (-0.004)

( ) = error.
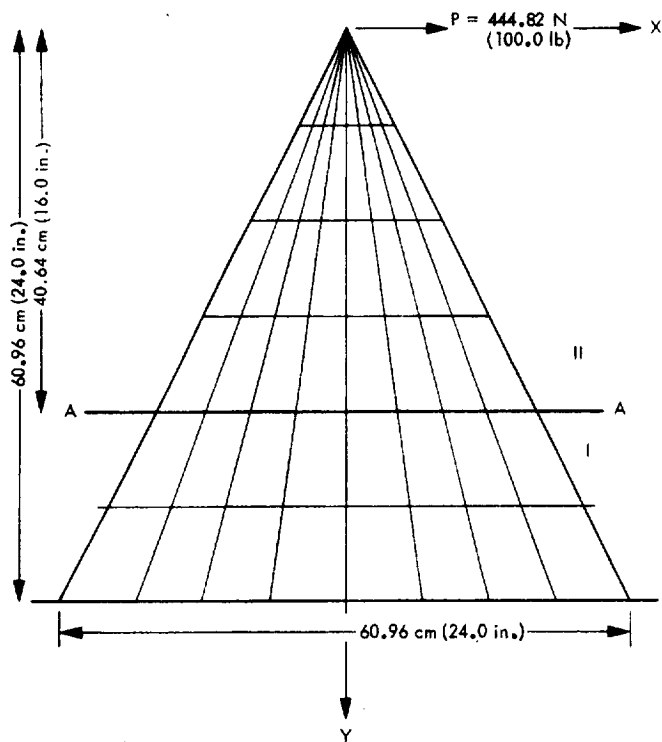
Fig. A-1. Plane stress finite element model of a force acting at the end of a wedge

"a", THEORETICAL (REF. 24)

"b$_I$" and "b$_{II}$", CONVENTIONAL BEST FIT STRAIN, SEC. II

"c", GENERATED BEST FIT STRAINS, SEC. III
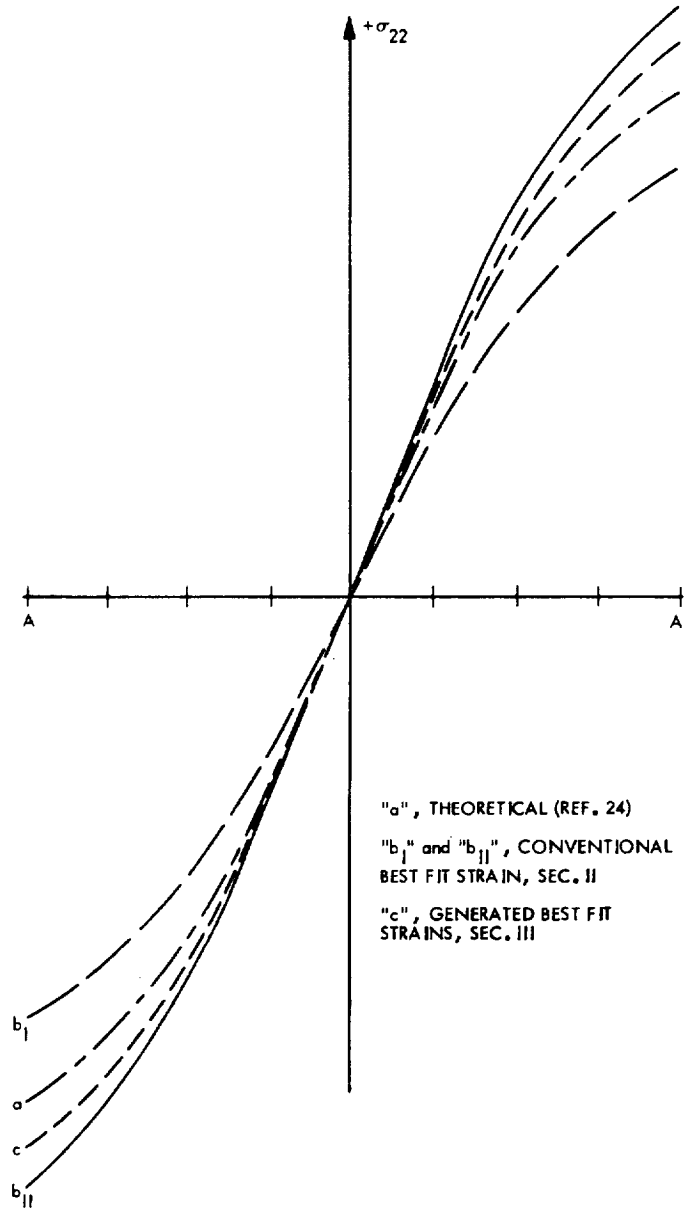
Fig. A-2. Normal stresses σ_{22} at A-A
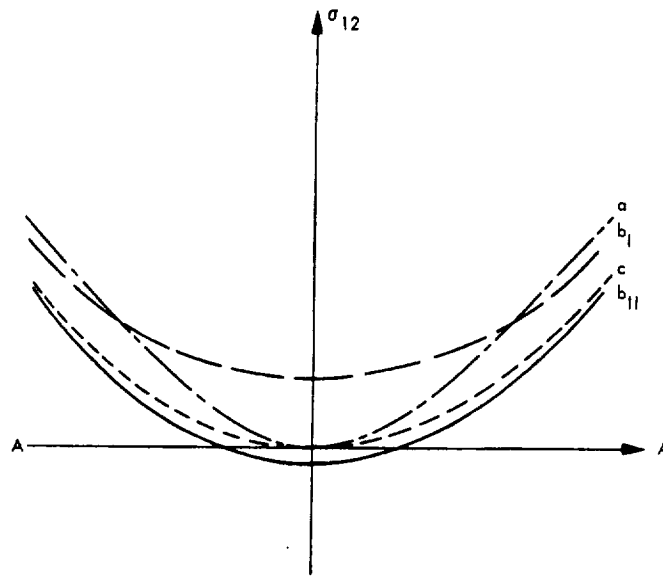
"a", THEORETICAL (REF. 24)

"b_I", "b_{II}", CONVENTIONAL BEST FIT STRAINS, SEC. II

"c", GENERALIZED BEST FIT STRAINS, SEC. III

Fig. A-3. Shear stresses σ_{12} at A-A

OUTSIDE CYLINDER
E = 103.423 GN/m^2
(15 × 10^6 lb/in.^{2})
μ = 0.3
α = 12 × 10^{-6} cm/cm/°C
(6.67 × 10^{-6} in./in./°F)

INSIDE CYLINDER
E = 206.846 GN/m^2
(30 × 10^6 lb/in.^{2})
μ = 0.33

5.08 cm (2 in.)

15.24 cm
(6 in.)

22.86 cm
(9 in.)
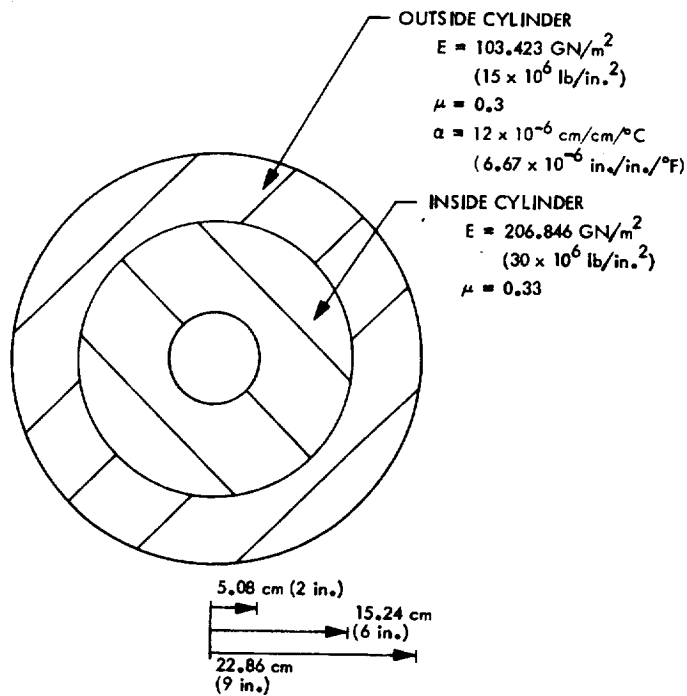
Fig. A-4. Two-cylinder shrink fit
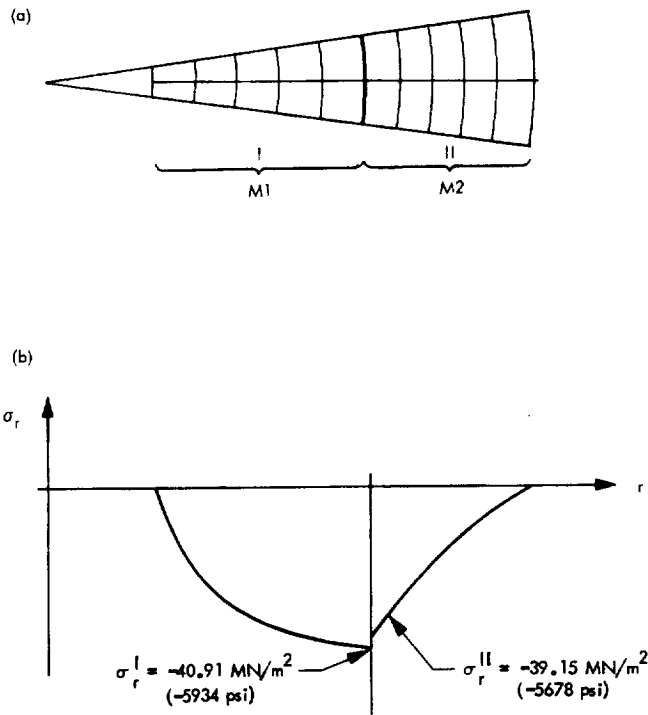
Fig. A-5. (a) Plane stress finite element model of two-cylinder shrink fit, (b) radial stress distribution
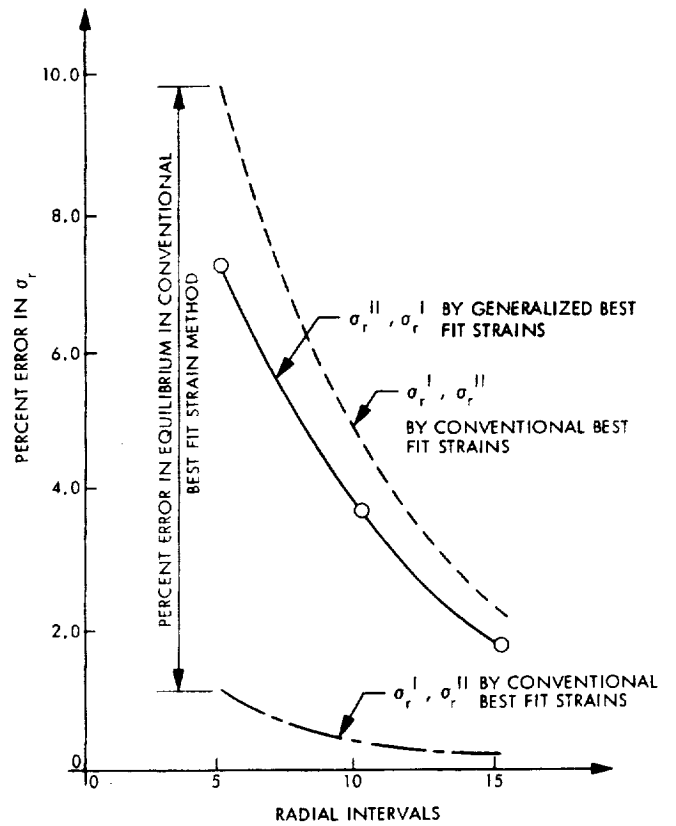
Fig. A-6. Error convergence in σ_r by the conventional and the generalized best fit strain

APPENDIX B

COMPOSITION OF THE SUBSTRATE MATERIALS

The five substrate materials tested in this program are:

(1) Kapton-H: a polyimide film made by E. I. DuPont DeNemours and Co.(Type 300H, from Mill Roll 04493). It was obtained with a thickness of 0.00762 cm (0.003 in.) in a roll 30.48 cm (12 in.) wide.

(2) Kapton-F: a laminated film made by DuPont, consisting of a 0.00508-cm (0.002-in.) layer of Kapton-H sandwiched between 2 layers, each 0.00127 cm (0.0005 in.) thick, of Teflon (Type 300F 929, from Mill Roll 00809). It was obtained with a total thickness of 0.00762 cm (0.003 in.) in a roll 30.48 cm (12 in.) wide.

(3) Teflon: a fluorinated ethylene propylene film made by DuPont (Type FEP 500A). The material was obtained with a thickness of 0.0127 cm (0.005 in.) in a roll 60.96 cm (24 in.) wide. It was not possible to determine the mill roll from which it was cut.

(4) Tedlar: a polyvinyl fluoride film made by DuPont (Type 200 SG 40 TR, from Slit Roll 7E014140). It was obtained with a thickness of 0.00508 cm (0.002 in.) in a roll 30.

(5) PG-402 0/0: a fiberglass-reinforced polyimide made by the Mica Corporation, Culver City, Cal. (from Lot 11974-2028-1). The symbol 0/0 refers to no copper cladding. It was obtained in 91.44 x 45.72 cm (36 x 18 in.) sheets with a thickness of 0.00635 cm (0.0025 in.). The 1080 plain weave fiberglass cloth had a warp of 60 and a fill of 47; an amino silane finish was put on the cloth for better wetting during the fabrication of the PG-402.

APPENDIX C

COEFFICIENT OF THERMAL EXPANSION FOR SUBSTRATE MATERIALS:
TEST PROCEDURE AND INSTRUMENTATION

The linear expansion coefficients were computed from measurements of the specimen length variation with temperature. A brief description of the methods and instruments follows. The test apparatus was a quartz tube dilatometer (Figs. C-1 and C-2) built in accordance with methods explained in ASTM E-228. The test specimens were held in tension by Invar grips attached to concentric fused silica tubes. Changes in the relative positions of the upper ends of the tubes (representing changes in length) were recorded with a 0.000254 cm (0.0001 in.) dial indicator.

The lower end of the tube was temperature-stabilized between -195.6 and 204.4°C (-320 and 400°F). The chamber was then sealed and a dry helium purge was maintained inside the tubes. The chamber temperature was stabilized electrically and monitored by three thermocouples. The effects of dimensional changes in the low expansion Invar grips were further minimized by the self-compensating design.

The test specimens were approximately 9.398 cm (3.7 in.) long with a maximum width of 2.286 cm (0.9 in.) and a maximum thickness of 0.2286 cm (0.090 in.).

The test procedure was to adjust the chamber temperature until the specimen temperature was constant. Accuracy of the measurement was approximately $\pm 5 \times 10^{-5}$ cm/cm over the full temperature range.
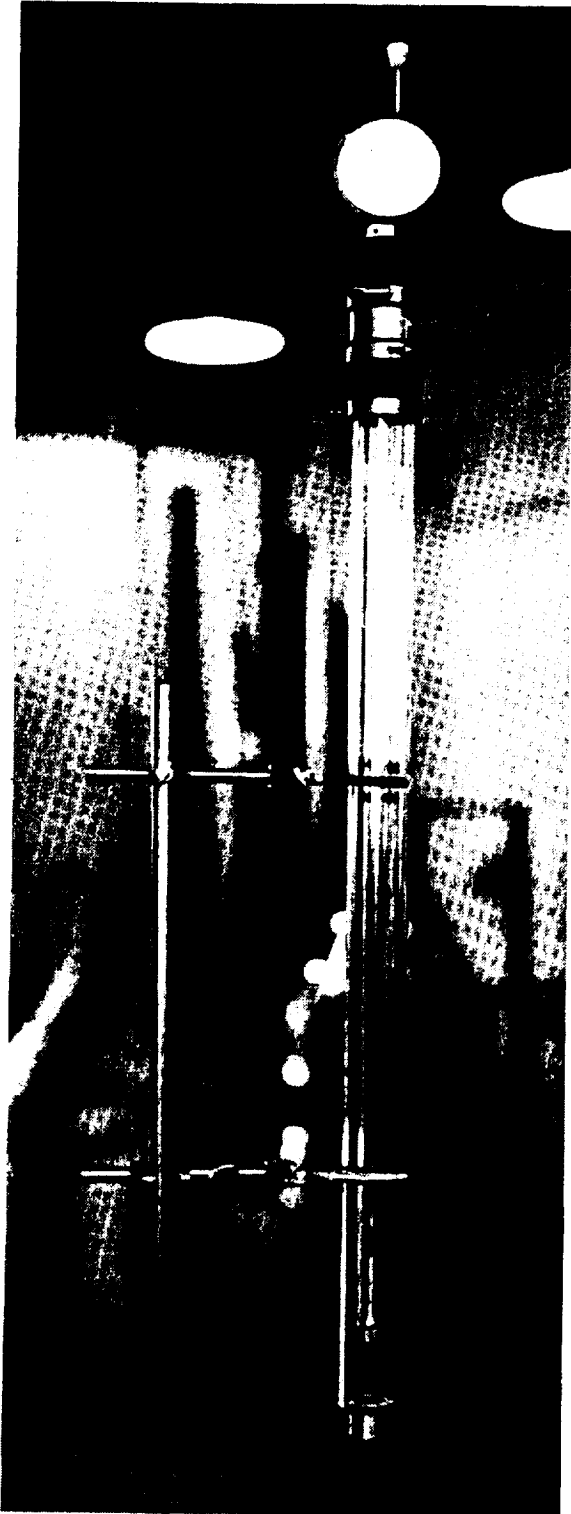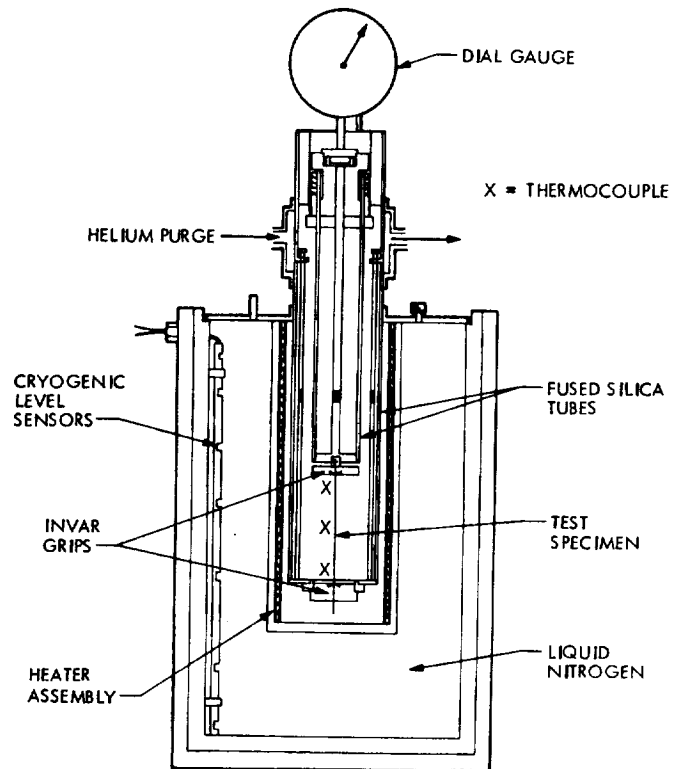
Fig. C-1. Quartz tube dilatometer

Fig. C-2. Schematic diagram of quartz tube dilatometer and heater

APPENDIX D

TEST SETUP AND SPECIAL TECHNIQUES
USED IN MECHANICAL PROPERTY MEASUREMENTS

I. TEST SETUP

The mechanical tests were performed on an Instron tensile testing machine. Figures D-1 and D-2 show photographs of the machine, with a typical polymer sample in the grips of the clamping device in the test chamber. Liquid nitrogen was used as the coolant for low-temperature measurements, in preference to carbon dioxide, which was found to produce anomalous surface effects on the samples.

Special grips were designed and made out of aluminum for applying a tensile load to the test specimens (see Fig. D-1). About two to three inches (depending upon material thickness) of material was wrapped around a 1.27-cm (0.5-in.) diameter spool which was inserted in a clamping device. To increase the coefficient of friction, the spool surface was sandblasted. The clamps were locked in place by a thumb screw in the bottom grip and by an Allen cap screw in the top grip. The test specimen was in the line of applied force between the cross head and the load cell in the top of the Instron tensile machine.

Each clamping device was fastened to a ball socket joint which provided an effective universal joint immediately adjacent to the specimen grips. From studies of the precision mechanical properties of materials, it was shown that this method of specimen alignment minimizes any bending in the test specimen. A minimum load was always maintained to preserve the axiality of the specimen.

II. PHOTOGRAPHIC METHOD FOR STRAIN MEASUREMENT

Because the test specimens were very thin polymer films, Poisson's ratio measurements using conventional strain gauges resulted in considerable errors. The errors arise from the fact that the gauge stiffness is comparable to the specimen stiffness. Thus, to obtain more accurate strain measurements, a special photographic method was developed. First, a reference pattern of fiducial crosses was inked on the surfaces of each test specimen, as shown in Fig. D-3. The total array of the crosses, on 0.254-cm (0.1-in.) centers, occupied an area 2.54 by 10.16 cm (1 by 4 in.) long. Several methods of applying the patterns were evaluated before a silk screen method was selected.

When the test specimen is loaded in the testing machine, these fiducial patterns deform laterally and longitudinally. The relative lateral to longitudinal deformation of a central portion away from the edges of each specimen provided a measure of Poisson's ratio. The deformed patterns were photographed for purposes of later measurements. A tripod-mounted 35-mm Pentax camera fitted with a 100-mm f/4 bellow Takuman lens and a shutter speed of 1/8 sec was used for this purpose.

All tests, except those at 25°C, were made inside an environmental chamber. Photographs from 38.1 cm (15 in.) were taken through a double glass window (specimen to camera). Figure D-4 shows a typical distortion of the fiducial patterns for Kapton-H for conditions of zero, 14, and 32% strains at 100°C. The distorsion is much more pronounced in the case of the Teflon, Fig. D-5. In the latter, appreciable distortion occurs up to 125% strain without specimen breakage.
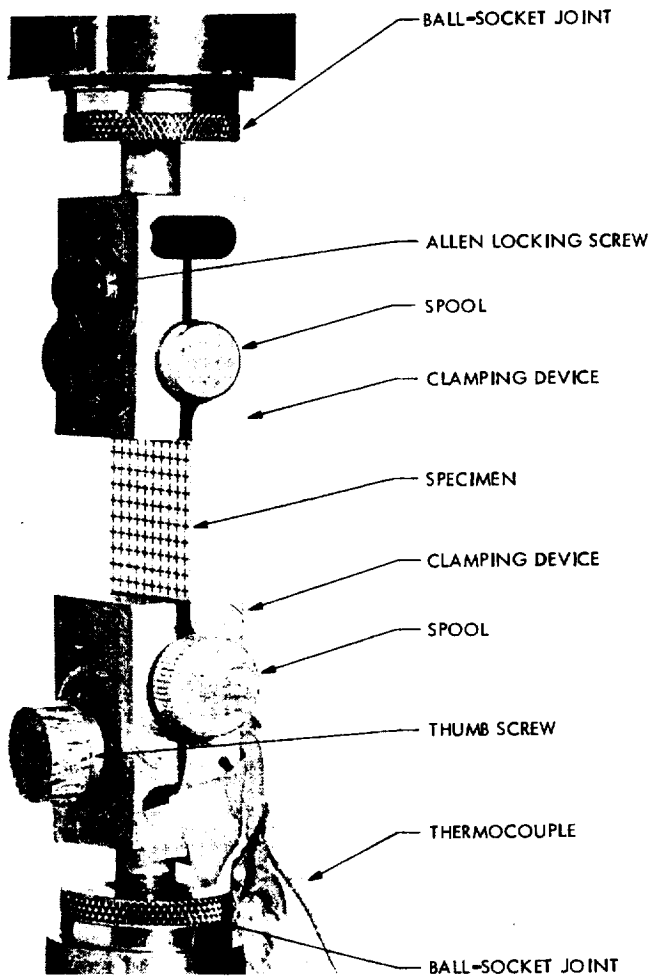
Fig. D-1. Tensile testing machine:
2.54-cm (1-in.) gauge length specimen
mounted in grips
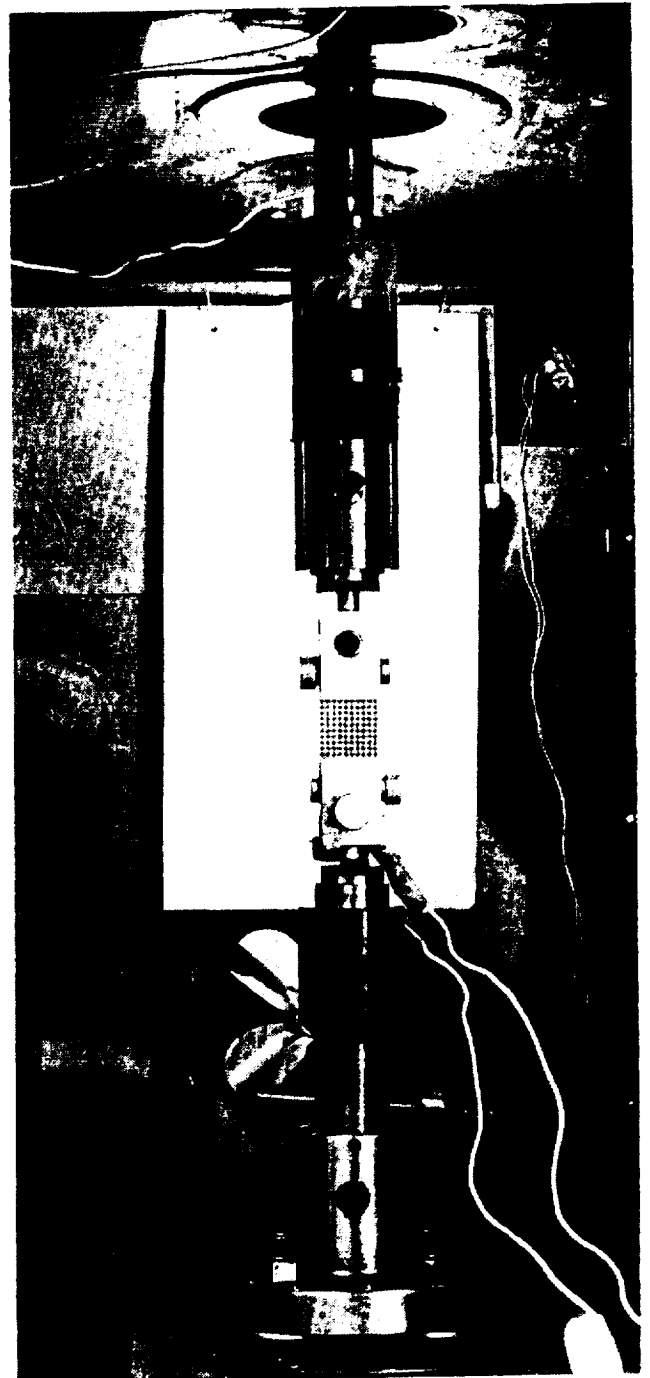
Fig. D-2. Tensile testing machine:
2.54-cm (1-in.) gauge length specimen
mounted in testing chamber
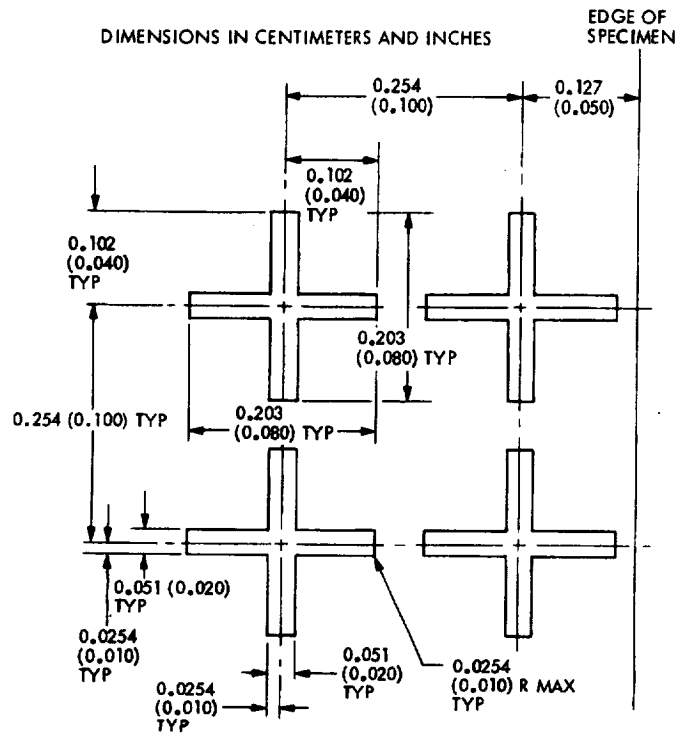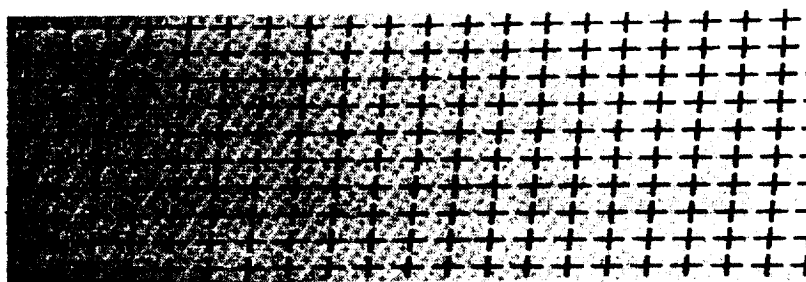
Fig. D-3. Dimensions of "plus signs" used
as fiducial pattern
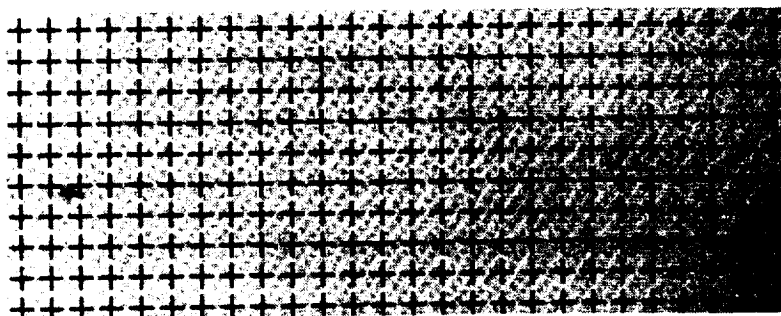
(a) NO STRAIN
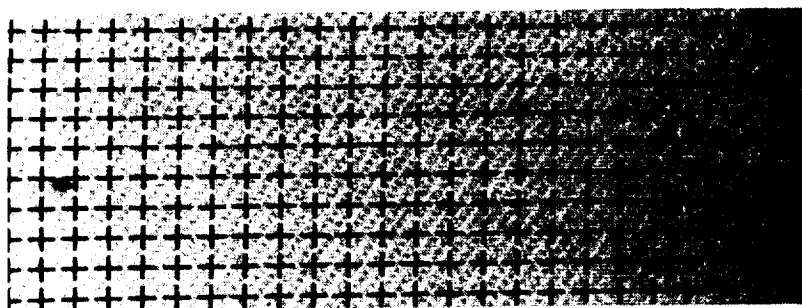
(b) 14% STRAIN

(c) 32% STRAIN

Fig. D-4. Distortion of the baseline fiducial
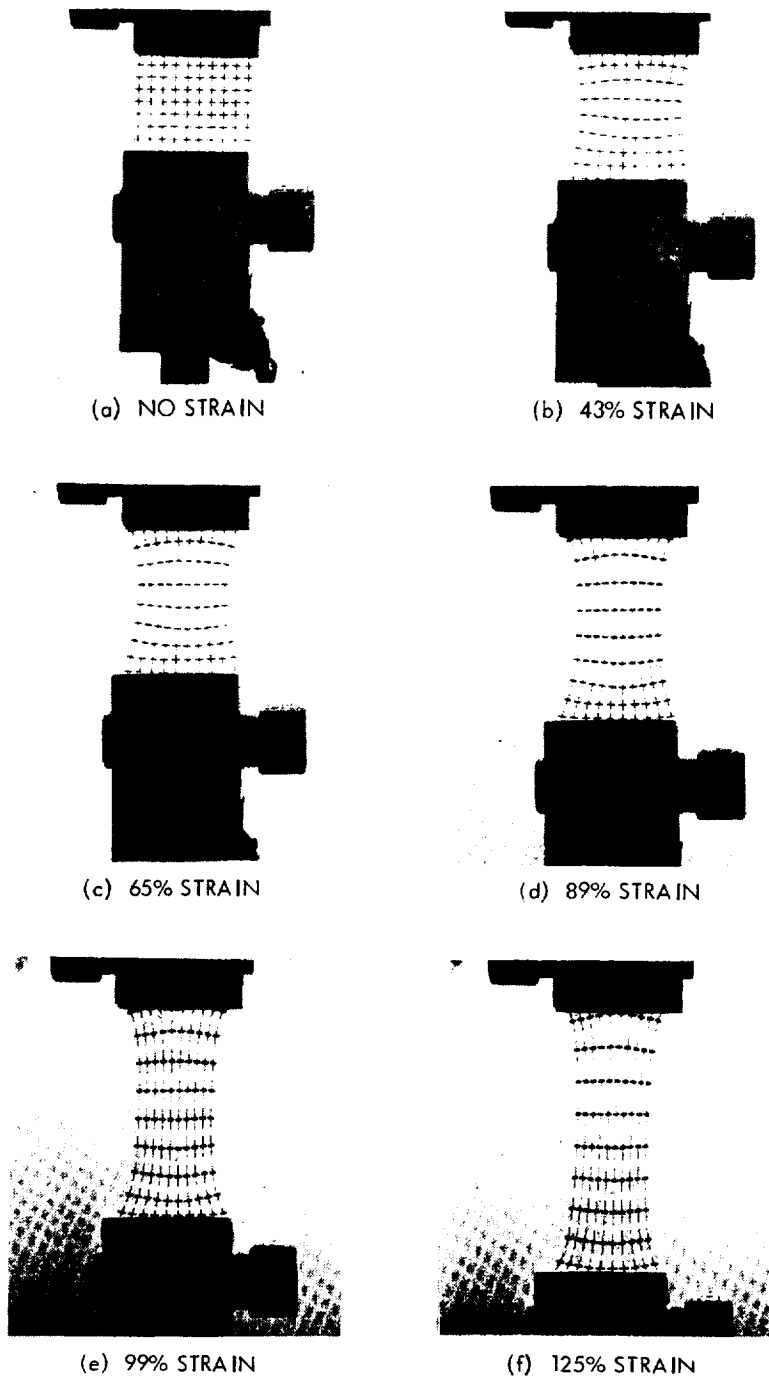patterns for Kapton-H, 10.2-cm (4-in.) gauge
length, 100°C

(a) NO STRAIN   (b) 43% STRAIN

(c) 65% STRAIN   (d) 89% STRAIN

(e) 99% STRAIN   (f) 125% STRAIN

Fig. D-5. Distortion of the baseline fiducial patterns for Teflon, 2.54 cm (1-in.) gauge length, -100°C

APPENDIX E

PROCEDURE FOR SPECIMEN PREPARATION
FOR MECHANICAL PROPERTY TESTS

Test specimens 30.48 cm (12 in.) long by 2.54 cm (1 in.) wide were cut using a double-bladed tool developed for this program. The cutting apparatus (Fig. E-1) consists of a double-grooved base plate, a clamping bar, and a block for mounting two razor blades. Figure E-2 shows the apparatus assembled preparatory to cutting a Kapton-H specimen.

A strip of material several inches wide is placed upon the base plate. The clamping bar is then placed over it, positioned by two locating pins at the ends. The block holding the razor blades is then drawn along the clamping bar with a slow, steady motion. In order to avoid splits or tears at the edges of the specimens, the razor blades were changed frequently. Cut edges were examined with an electron microscope, but the shallow depth of focus prevented satisfactory analysis. Random specimens were examined in the scanning electron microscope, after application of a thin coating of carbon to render the surfaces electrically conductive. Typical edge effects are shown in Figs. E-3 through E-7. Tedlar (Fig. E-3) had the "cleanest" cut because it had the smoothest cut face and no burr at the bottom where the blade left the material. Teflon edges (Fig. E-4) were marked by a pronounced burr at the bottom surface and a slightly rough cut face. Figure E-5 (Kapton-H) showed a slightly serrated cut edge with only a very small burr. Kapton-F (Fig. E-6) also showed a burr at the bottom surface of the outer layer of Teflon. None of the unreinforced polymer specimens showed edge defects that could be considered as sources of premature failure. The cut edge of PG-402 (Fig. E-7) was very rough because of the fiberglass content.
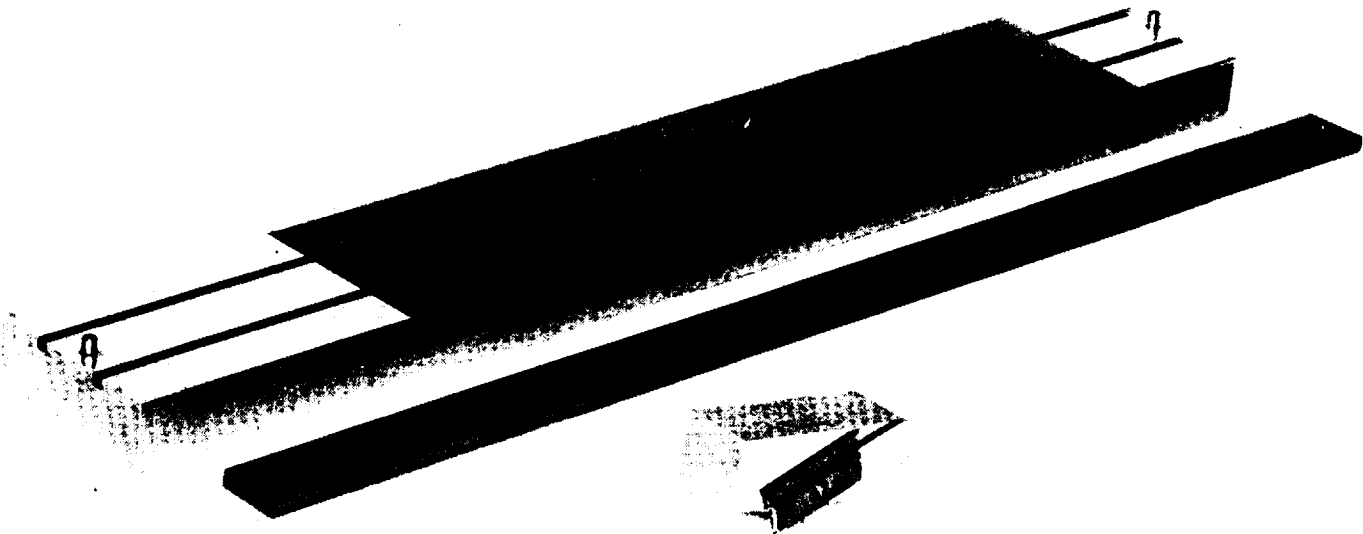
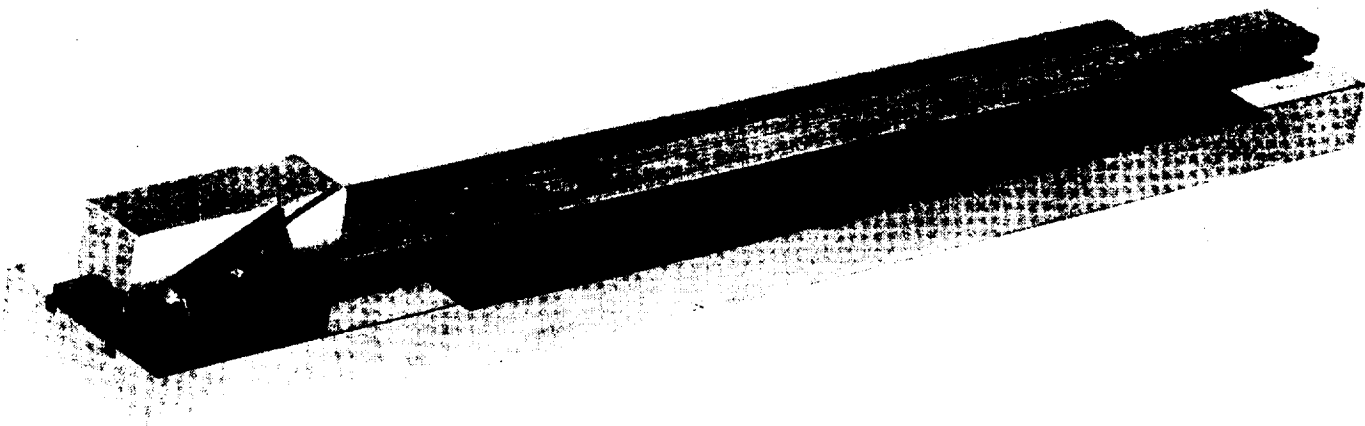Fig. E-1. Apparatus for cutting specimens, disassembled

Fig. E-2. Apparatus for cutting specimens, assembled
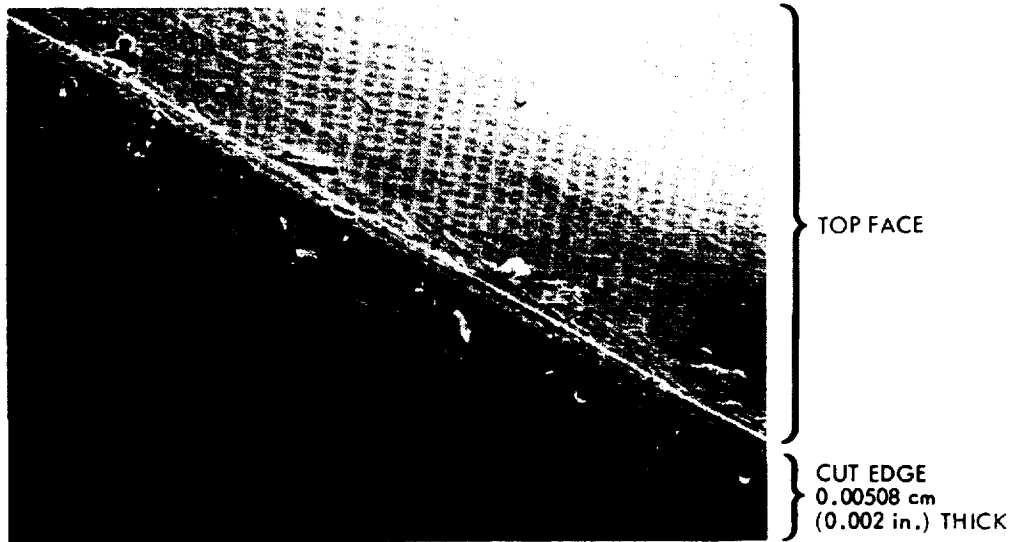
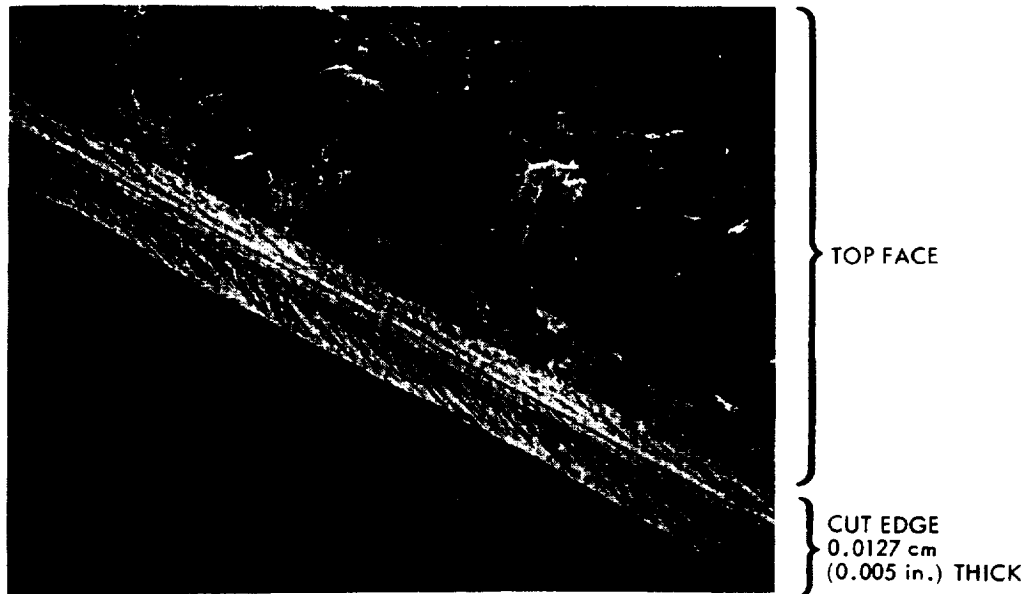Fig. E-3. Tedlar: cut edge of specimen (scanning electron microscope, 190X)

Fig. E-4. Teflon: cut edge of specimen (scanning electron microscope, 250X)
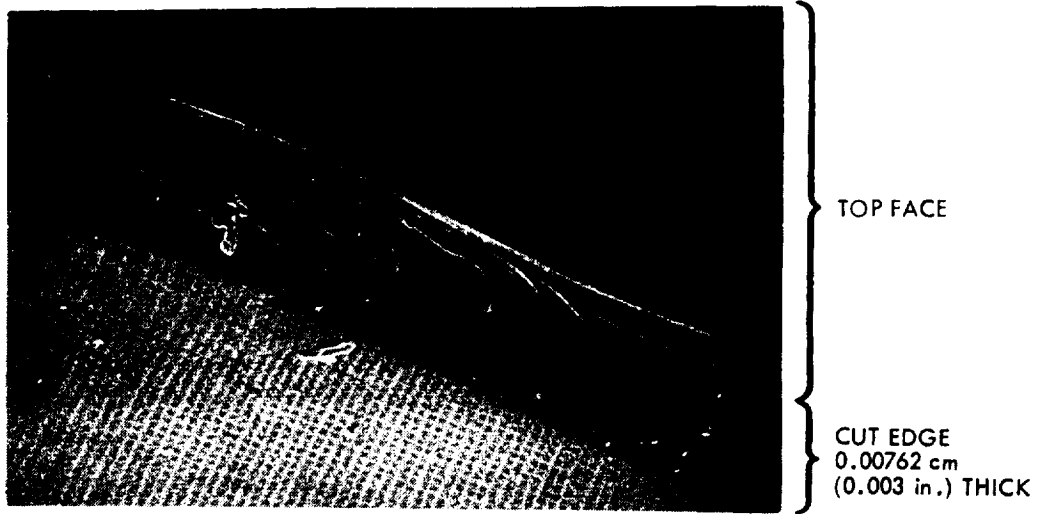
TOP FACE

CUT EDGE
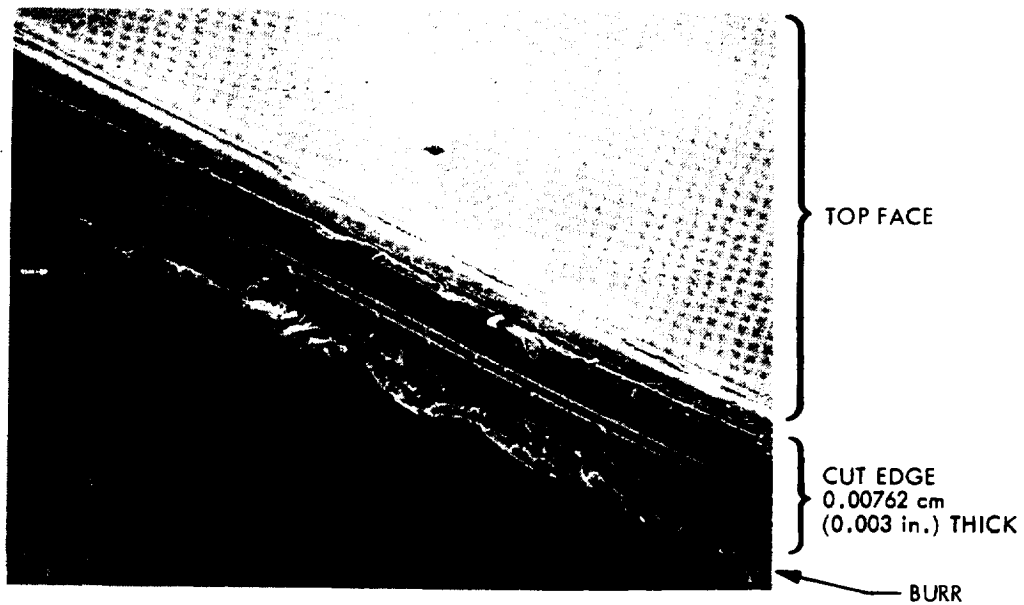0.00762 cm
(0.003 in.) THICK

Fig. E-5. Kapton-H: cut edge of specimen (scanning electron microscope, 225X)

TOP FACE

CUT EDGE
0.00762 cm
(0.003 in.) THICK

BURR

Fig. E-6. Kapton-F: cut edge of specimen (scanning electron microscope, 210X)
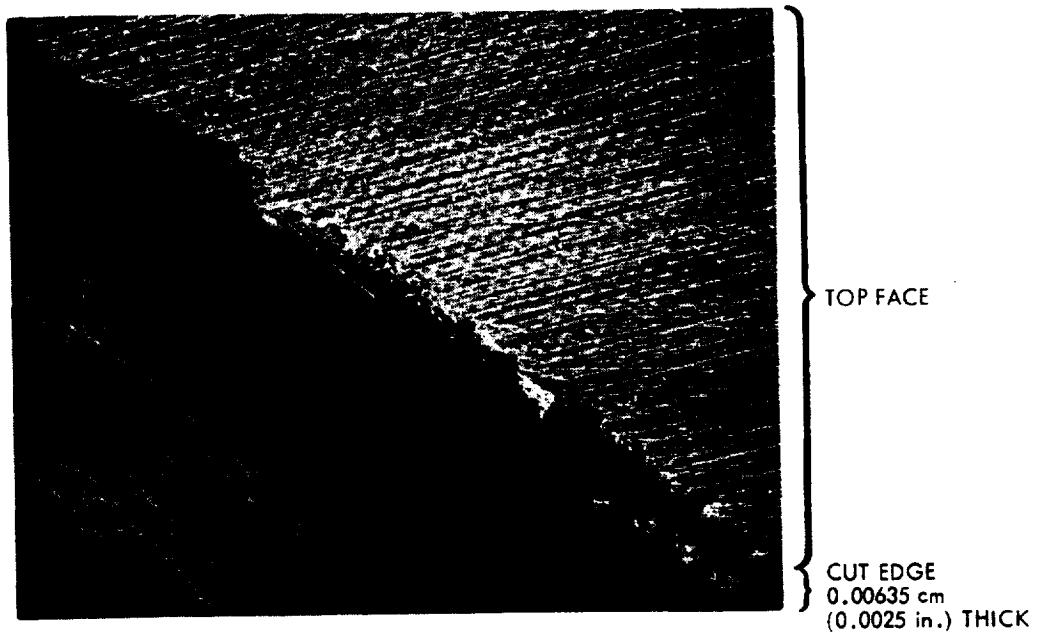
TOP FACE

CUT EDGE
0.00635 cm
(0.0025 in.) THICK

Fig. E-7. PG-402: cut edge of specimen (scanning electron microscope, 100X)

REFERENCES

1. Salama, M. A., Rowe, W. M., and Yasui, R. K., "Stress Analysis and Design of Silicon Solar Cell Arrays and Related Material Properties," in Conference Record of the Ninth IEEE Photovoltaic Specialists Conference, pp. 146-157, Silver Spring, Md, May 1972.

2. Salama, M. A., Rowe, W. M., and Yasui, R. K., _Thermoelastic Analysis of Solar Cell Arrays and Their Material Properties_, Technical Memorandum 33-626, Jet Propulsion Laboratory, Pasadena, Calif., Sep. 1973.

3. Hartzman, M., "Stress-Strain Relations for Materials with Different Tension, Compression Yield Strengths," _J. AIAA_, Vol. II, No. 3, pp. 378-379, Mar. 1973.

4. Utku, S., and Akyuz, F. A., _ELAS - A General-Purpose Computer Program for the Equilibrium Problems of Linear Structures: User's Manual_, Tech-Report 32-1240, Vol. I, Jet Propulsion Laboratory, Pasadena, Calif., Feb. 1968.

5. Gupta, K. K., Akyuz, F. A., and Heer, E., _VISCEL - A General-Purpose Computer Program for Analysis of Linear Viscoelastic Structures: User's Manual_, Technical Memorandum 33-466, Vol. I, Rev. 1, Jet Propulsion Laboratory, Pasadena, Calif., Oct. 1972.

6. "Mechanical Design Data for Teflon Fluorocarbon Resins," Plastic Department, DuPont Company, Wilmington, Del.

7. Clark, F. M., _Insulating Materials for Design and Engineering Practice_, John Wiley, New York, p. 603, 1962.

8. Nielsen, L. E., _Mechanical Properties of Polymers_, Van Nostrand Reinhold Co., 1962.

9. Clark, E. S., "Morphology and Physical Properties of Crystalline Polymers," _Polymer Preprints_, Vol. 14, No. 1, pp. 88-91, May 1973.

10. Parrish, M., and Brown, N., "Environmental Effects on the Tensile Deformation of Polymers at Low Temperatures," _J. Macromal Sci-Phys._, B8 (3-4), p. 655, 1973.

11. Olf, H. G., and Peterlin, A., "Crazing in a Crystalline Polymer (Isotactic Polypropylene) and the Role of N_2O_2 and CO_2 as Crazing Agents," _Polymer_, Vol. 14, pp. 78-79, Feb. 1973.

12. Zienkiewicz, O. C., _The Finite Element Method in Engineering Science_ McGraw-Hill, New York, 1971.

13. Wilson, E. L., "Finite Element Analysis of Two-Dimensional Structures," Ph. D. Thesis, University of California, Berkeley, 1963.

14. Utku, S., "Best Fit Stress Computation in Displacement Methods," paper presented in the Discrete and Continuum Concepts in Micro and Macro Mechanics, EMD Specialty Conference, ASCE, North Carolina State University, Raleigh, N. C., Nov. 1967.

15. Oden, J. T., and Brauchli, H. J., "On the Calculation of Consistent Stress Distribution in Finite Element Applications," Int. J. Numer. Meth. Eng., Vol. 3, pp. 317-325, 1971.

16. Stein, E., and Ahmad, R., "On the Stress Computation in Finite Element Models Based Upon Displacement Approximations," Comp. Meth. Appl. Mech. Eng., Vol. 4, pp. 81-96, 1974.

17. Stricklin, J. A., "Computation of Stress Resultants From the Element Stiffness Matrices," J. AIAA, Vol. 4, pp. 1095-1096, 1966.

18. Navaratna, D. R., "Computation of Stress Resultants in Finite Element Analysis," J. AIAA, Vol. 4, pp. 2058-2060, 1966.

19. Argyris, J. H., and William, K. J., "Some Considerations for the Evaluation of Finite Element Models," 2nd International Conference on Structural Mechanics and Reactor Technology, Berlin, 1973.

20. Utku, S., ELAS - A General-Purpose Computer Program for the Equilibrium Problems of Linear Structures, Vol. II, Documentation of the Program, Technical Report 32-1240, Jet Propulsion Laboratory, Pasadena, Calif., Sept. 1969.

21. Utku, S., Rao, M. S. M., and Dvorak, G., ELAS65 Program for Elastic-Thermo-Plastic Solids and Structures, Structural Mechanics Series No. 15, School of Engineering, Duke University, Durham, N. C., 1973.

22. Utku, S., Tarn, J., and Dvorak, G., ELAS55 Program for Thermo-Visco Elastic-Plastic Solids and Structures, Structural Mechanics Series No. 21, School of Engineering, Duke University, Durham, N. C., 1974.

23. Nay, R. A., and Utku, S., "An Alternative for the Finite Element Method," Variational Methods in Engineering, Vol. II, Department of Civil Engineering, Southampton University Press, pp. 3/62-3/74, 1973.

24. Timoshenko, S., Strength of Materials, Part II, 3rd ed., D. Van Nostrand, 1956.